C. R. Physique 17 (2016) 332–356

Contents lists available at ScienceDirect

Comptes Rendus Physique

www.sciencedirect.com

Condensed matter physics in the 21st century: The legacy of Jacques Friedel

The Peierls instability and charge density wave in one-dimensional electronic conductors

Instabilité de Peierls et onde de densité de charge dans les conducteurs électroniques à une dimension

Jean-Paul Pouget *

Laboratoire de physique des solides, UMR 8502, CNRS, Université Paris-Sud, 91405 Orsay, France

ARTICLE INFO

Article history:
Available online 17 December 2015

Keywords:
One-dimensional electronic conductors
Peierls transition
Charge density wave
Kohn anomaly
CDW elasticity, plasticity and pinning
Friedel oscillations

Mots-clés :
Conducteurs électroniques à une dimension
Transition de Peierls
Onde de densité de charge
Anomalie de Kohn
Elasticité, plasticité et accrochage des ondes de densité de charge
Oscillations de Friedel

ABSTRACT

We review salient structural and electronic features associated with the concomitant Peierls–charge density wave (CDW) instabilities observed in most one-dimensional (1D) inorganic and organic electronic conductors. First of all, the genesis of these concepts is placed in an historical perspective. We then present basic experimental facts supporting the general description of these 1D electron–phonon coupled systems developed in the 1970s. In this framework we shall consider in particular the role of 1D fluctuations on both lattice and electronic degrees of freedom, and of the inter-chain Coulomb coupling between CDWs in stabilizing in 3D the Peierls transition at finite temperature. We also clarify, in relation with experimental findings, the various conditions of adiabaticity of the electron–phonon coupling. Finally we illustrate by recent structural measurements the pioneering work of Jacques Friedel on CDW elasticity and plasticity and CDW pinning to defects through the appearance of Friedel oscillations.

RÉSUMÉ

Nous passons en revue les principaux aspects structuraux et électroniques de l'instabilité Peierls–onde de densité de charge (ODC) observée dans la plupart des conducteurs inorganiques et organiques à une dimension (1D). Nous commençons par replacer la genèse de ces concepts dans une perspective historique. Puis nous présentons les faits expérimentaux à la base de la description générale de ces systèmes 1D couplés électron–phonon développée à partir des années 1970. Dans ce cadre, nous considérerons en particulier l'effet des fluctuations 1D sur les degrés de liberté structuraux et électroniques et le rôle du couplage coulombien inter-chaine dans le mécanisme de stabilisation 3D de la transition de Peierls à température finie. Nous clarifions aussi, en relation avec les données expérimentales, les différentes conditions d'adiabaticité du couplage électron–phonon. Finalement, nous illustrons avec des mesures structurales récentes les travaux

* Corresponding author. Tel.: +33 169156046; fax: +33 169156936.
E-mail address: jean-paul.pouget@u-psud.fr.

http://dx.doi.org/10.1016/j.crhy.2015.11.008

pionniers de Jacques Friedel sur l'élasticité et la plasticité des ODC et leur accrochage aux défauts via la formation d'oscillations de Friedel.

1. Historical perspective

The framework used nowadays to describe the metal–insulator (M–I) transition occurring in 1D conductors by the setting of a $2k_F$ periodic lattice distortion (PLD) was established by Peierls [1] and Fröhlich [2] in the mid-1950s (k_F is the Fermi wave vector of the 1D electron gas, which amounts in reciprocal chain unit, d^*, to one quarter of the charge ρ per site). However, as pointed out by Friedel [3], the physics underlying these works had already emerged in the beginning of the 1930s when Jones [4] showed that superstructures can be stabilized in normal metals and alloys when the Fermi sphere touches a maximum number of Brillouin zone boundaries issued from the superstructure reciprocal lattice periodicities. More precisely, Peierls calculated in 1930 [5] the energy spectrum of a free electron gas submitted to an external sinusoidal potential. He found that the effect of a periodic potential of wave number q is to open an energy gap (2Δ) in the band structure at wave vectors $\pm q/2$. For a 1D electronic structure, there is a full gap opening at the Fermi level for $\pm k_F$ if the potential wave number amounts to $q = 2k_F$ (see Fig. 1). In addition if, as considered by Peierls and Fröhlich in the 1950s, the potential is set by a $2k_F$ PLD, the lattice modulation trigs an insulating ground state. However, Peierls first demonstrated that the gap opening is stable whatever the magnitude of the $2k_F$ PLD and, for this reason, the metal–insulator (M–I) transition that results is now called a Peierls transition (the argument of Peierls was given for an half-filled band where, with $\rho = 1$, $2k_F = d^*/2$ is commensurate, but the result can be easily generalized whatever ρ). Independently of Peierls' work, Fröhlich [2] then Kuiper [6] developed the thermodynamics of the M–I transition due to the setting of a $2k_F$ PLD. Interestingly, their (mean-field) theory gave at $T = 0$ K a (half) energy gap Δ_{MF}, which exponentially depends on the inverse of the dimensionless electron–phonon coupling constant λ (expression (2.53) in Ref. [2]):

$$\Delta_{MF} \sim E_F e^{-1/\lambda} \tag{1}$$

In addition, Δ_{MF} was found to be proportional to the (mean-field) critical temperature of the M–I transition, T_P^{MF} (expression (3.1) in Ref. [6]):

$$\Delta_{MF} = 1.75 k_B T_P^{MF} \tag{2}$$

λ and T_P^{MF} will be more precisely defined by relations (22) and (23) below in section 2.3. Relations (1) and (2) are similar to expressions obtained later in 1957 for the superconducting gap and critical temperature in the BCS theory of superconductivity (in the BCS theory, the Debye phonon energy replaces the Fermi energy, E_F, in expression (1)). However the analogy between the Peierls–Fröhlich and BCS theories was only noticed a few years later [7], but not really commented in the literature at that time. Then the pioneering works of Peierls, Fröhlich and Kuiper were forgotten and the thermodynamics of the Peierls transition was re-derived (using a more transparent formalism) independently several times during the 1970s [8,9] when the study of the M–I phase transition became a major subject of research.

In addition, Fröhlich showed that because of the electron–phonon coupling, the PLD induces a $2k_F$ periodic charge density wave (CDW) modulation of the electronic density whose charge can couple with an external electric field, E. In this framework, the main purpose of Fröhlich's work [2] was to provide an explanation for the zero-resistance state of superconductors by showing, using a 1D model, that the (incommensurate) $2k_F$ CDW could collectively slide under the action of E and thus behaves as a superfluid. In this respect, Fröhlich was the first to introduce in 1954 the concept of CDW as the counterpart of the PLD and to notice that the two modulations should stabilize each other. Later, Overhauser proposed [10] the formation of pure electronic CDWs in a simple metal. However, Friedel provided physical arguments [3] suggesting that it is unlikely that an electronic CDW could be stabilized in the absence of a PLD.

The $2k_F$ PLD/CDW instability driving the Peierls transition was first observed in 1973 in the framework of an X-ray diffuse scattering investigation of the 1D conductor $K_2Pt(CN)_4Br_{0.3}\cdot 3H_2O$ (KCP) [11]. Note that at the same time, electron diffraction studies provided evidence of a PLD/CDW modulation in layered metallic transition-metal di-chalcogenides MX_2. However, if the Peierls mechanism provides a clear explanation of most of the M–I transition observed in 1D conductors, the microscopic origin of the PLD/CDW instability of MX_2 compounds is still debated. Then in the following years, the $2k_F$ PLD/CDW Peierls transition was observed in charge-transfer organic salts such as TTF–TCNQ (TTF, TCNQ and the other organic molecules quoted in the text are defined in the chemical index at the end of the paper), in the blue bronze $K_{0.3}MoO_3$ and in the transition-metal tri-chalcogenide $NbSe_3$ (see section 2). Finally, the Fröhlich type of collective sliding of a $2k_F$ CDW under the action of large enough external electric fields was observed in the Peierls ground state of $NbSe_3$ [12] and $K_{0.3}MoO_3$ [13].

It is also interesting to remark that before the work of Peierls, Fröhlich and Kuiper, Slater proposed in 1951 [14] that the staggered exchange potential due to anti-ferromagnetic (AF) order could similarly drive a M–I transition in a half-filled ($\rho = 1$) 1D electronic system because the magnetic periodicity of wave number $d^*/2$ amounts to twice the Fermi wave vector of the 1D band, $2k_F$. Then it was shown later that more general $2k_F$ Fermi surface (FS) nesting processes could

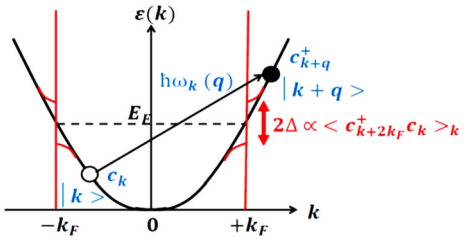

Fig. 1. 1D Electron dispersion together with an electron–hole $\hbar\omega_k(q)$ excitation process. The Peierls gap 2Δ that develops below T_P is expressed as a function of the creation ($c^+_{k+2k_F}$) and annihilation (c_k) electron operators involved in the $q = 2k_F$ excitation process.

stabilize either a spiral [15] or an oscillating [16] $2k_F$ spin density wave (SDW). Although SDWs stabilized by the FS nesting mechanism are known since more than half a century in 3D metals such as Cr [17], the type of M–I transition predicted by Slater was only observed in the 1980s in the Bechgaard salt $(TMTSF)_2PF_6$ [18]. However, recent diffraction experiments provide evidence that the insulating ground state of $(TMTSF)_2PF_6$ is in fact a mixture of $2k_F$ SDW and $2k_F$ CDW modulations [19]. Such a composite $2k_F$ modulated state was previously considered by Overhauser [20].

The organic salt TTF–TCNQ not only undergoes a $2k_F$ PLD/CDW Peierls instability (on the TCNQ stack), but also an additional instability (on the TTF stack) at twice the $2k_F$ wave vector [21]. Since the $4k_F$ wave vector amounts to ρd^*, the associated PLD can be viewed as the lattice fingerprint of a Wigner charge localization (or $4k_F$ CDW) achieving a charge periodicity of $1/\rho$ in chain direction [22,23]. In the limit of infinite intra-site repulsion U, the $4k_F$ instability is analogous to the $2k_F^{SL}$ Peierls instability in a 1D spin-less electron gas. Note that the spin-less denomination is due to the fact that when U is infinite, a site is at most occupied by one fermion whose spin degree of freedom is thus irrelevant. Note that if k_F (in d^* units) remains defined for the 1D free electron gas by ρ /4, one has $k_F^{SL} = 2k_F$. Thus, in the presence of electron–phonon coupling, the 1D pseudo-fermion gas should develop a Peierls instability at the $2k_F^{SL} = 4k_F$ critical wave vector.

The $4k_F$ Wigner charge localization induces a spin–charge decoupling. Thus below the $4k_F$ PLD/CDW transition, the spins $S = 1/2$, generally coupled in an AF manner, remain available for an additional magnetic instability towards either $S = 1/2$ AF or $S = 0$ spin–Peierls (SP) ground states. In the latter case, in the presence of strong enough magneto-elastic coupling, the pairing of neighboring $S = 1/2$ into a singlet is achieved via a dimerization of the $4k_F$ 1D superstructure. This spin–lattice coupled instability, which is analogous to the electron–lattice coupled Peierls instability in a half-filled band, is called SP instability. More precisely, if spins 1/2 are coupled by transverse (XY) AF exchange interaction, the mechanism of the SP transition is formally equivalent to the mechanism of the Peierls transition in a half-filled band of spin-less fermions [24]. In the case of AF exchange Heisenberg coupling, the theory of the SP transition is more elaborate because the longitudinal exchange component introduces attractive interaction between the 1D pseudo-fermions [25]. In the SP ground state, the singlet spin pairing is stabilized by the dimerization of the $4k_F$ super-structure of localized $S = 1/2$. The superstructure of double periodicity that results implies the $2k_F$ critical wave number as for the Peierls transition. This means, when Coulomb repulsions progressively increase, that one passes continuously from the $2k_F$ Peierls instability to the SP instability. SP ground states have been detected both in organic (TTF–CuBDT, MEM–$(TCNQ)_2$ and Fabre $(TMTTF)_2PF_6$ salts) and inorganic ($V_{1-x}Cr_xO_2$, $CuGeO_3$) magnetic chain compounds.

2. The Peierls instability

1D organic and inorganic conductors generally crystallize in anisotropic structure made of relatively well decoupled stacks of molecules (see Fig. 13a below) or atomic clusters (see Fig. 14 below). Due to the segregated chain structure and the anisotropic overlap of p_π (d) orbitals in organic (inorganic) compounds, there is a weak inter-chain transfer integral $t_\perp$. If $t_\perp$ is negligible, the 1D band structure of dispersion $\varepsilon(k)$ is filled from $-k_F$ to $+k_F$ and the FS is composed of two points at $\pm k_F$ in the chain's direction (Fig. 1). The longitudinal wave vector $2k_F$ perfectly nests the 1D FS. Below we shall consider the situation where the transverse warping of the FS, due to $t_\perp$, is less than the thermal broadening of the FS above the 3D Peierls critical temperature T_P. Thus precisely for $t_\perp < \pi k_B T_P$, the one-electron Hamiltonian contains only 1D interactions:

$$H_{1D} = \sum_i \varepsilon(i) n_i + \sum_i t(i)\left(c_i^+ c_{i+1} + \text{h.c.}\right) \tag{3}$$

In this Hamiltonian, $\varepsilon(i)$ and $t(i)$ are respectively the energy of site i and the near-neighbor $i+1$ intra-chain transfer integral.

The simplest excitation, of energy $\hbar\omega_k(q) = \varepsilon(k+q) - \varepsilon(k)$, of the electronic structure create an hole in k together with an electron in $k+q$ (see Fig. 1). It consists of the formation of an electron–hole pair of wave vector q. The energy $\hbar\omega_k(q)$ is involved in the denominator of the electron–hole polarizability of the free electron gas (also called Lindhard response function), which is expressed by [18]:

$$\chi(q,\omega,T) = \frac{2}{L}\sum_k \frac{f(\varepsilon(k)) - f(\varepsilon(k+q))}{\varepsilon(k+q) - \varepsilon(k) - \hbar\omega + i\hbar\eta} \tag{4}$$

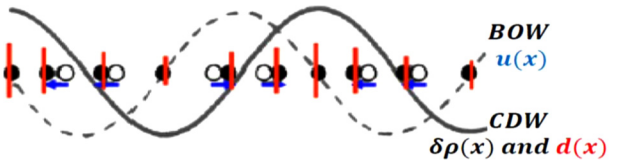

Fig. 2. $\pi/2$ phase shift between the BOW $u(x)$ and the CDW $\delta\rho(x)$. Note that the internal site deformation $d(x_i)$ behaves spatially as the CDW.

In expression (4), $f(\varepsilon(k))$ is the Fermi–Dirac function, L is the chain length and $\eta \to 0^+$ is a small quantity due to adiabatic continuity in the response process. For the FS nesting wave vector $q = 2k_F$ and a 1D linearized electron dispersion, expression (A.3) of the Appendix gives the analytical expression of $\chi(2k_F, \omega, T)$. The static ($\omega = 0$) electron–hole response function diverges in temperature as:

$$\chi(2k_F, \omega = 0, T) = N(E_F) \ln\left(\frac{2\gamma\varepsilon_c}{\pi k_B T}\right) \tag{5}$$

In (5), ε_c is a cut-off energy of the order of the Fermi energy E_F and $2\gamma/\pi \approx 1.13$. The logarithmic thermal divergence of expression (5) for $q = 2k_F$ drives the Peierls instability.

The Peierls gap 2Δ (Fig. 1) that opens at the Fermi level due to the $2k_F$ electron–hole instability is stabilized by the formation of a $2k_F$ PLD. In most of the cases, the PLD consists of a modulation of the bond distances. This forms a $2k_F$ bond order wave (BOW). The modulation of bond distances leads to a concomitant $2k_F$ modulation of the charge density or CDW as illustrated in Fig. 2. The CDW corresponds to a macroscopic condensate of $2k_F$ electron–hole pairs involved in the $\hbar\omega_k(q = 2k_F)$ excitation process; each of them is expressed as a function of creation ($c^+_{k+2k_F}$) and annihilation (c_k) electron operators (see Fig. 1). Thus the amplitude of the CDW modulation is given by the k average of all the $\hbar\omega_k(q = 2k_F)$ excitation processes:

$$\rho_{2k_F} = \langle c^+_{k+2k_F} c_k \rangle_k \tag{6a}$$

and its spatial dependence is expressed by:

$$\delta\rho(x) = \rho_{2k_F} \cos(2k_F x + \varphi) \tag{6b}$$

The amplitude of the CDW ρ_{2k_F} is proportional to the Peierls gap:

$$\rho_{2k_F} = \frac{N(E_F)}{\lambda}\Delta \tag{7}$$

The PLD is achieved by the coupling of the Hamiltonian (3) to phonons. Fig. 2 shows that the BOW that modulates the inter-site distance, $u(x)$, is in quadrature with the charge modulation (CDW) where $\delta\rho(x) \propto -\partial u(x)/\partial x$. The modulation of the charge on the site i formed by a molecule or an atomic cluster, $\rho + \delta\rho(x_i)$, should be accompanied by an intramolecular/cluster bond deformation in phase with the CDW: $d(x_i) \propto \delta\rho(x_i)$ (see Fig. 2). Both $u(x)$ or $d(x_i)$, which are in quadrature, stand for the PLD introduced in section 1. The BOW $u(x)$ is basically achieved by electron–phonon coupling with acoustic phonons that, via a change of the inter-site distances, modulate the transfer integral $t(i)$ in expression (3). The site deformation $d(x_i)$ is achieved by electron–phonon coupling with internal (optical) phonons that, via a change of the intramolecular/cluster distances, modulate the site energy $\varepsilon(i)$ in expression (3). For a free-electron system, the Peierls gap Δ is proportional to the amplitude of the PLD. Rigorously, one should introduce two Peierls gaps linearly related via the "bond" and "site" electron–phonon coupling constants, "g", to each component $u(x)$ and $d(x)$ of the PLD. In this case, the total Peierls gap is the sum in quadrature of the "bond" and "site" Peierls gaps.

2.1. Structural fluctuations

The Peierls instability is announced by the development below T_{1D} of $2k_F$ PLD fluctuations accompanied by a fluctuating CDW condensate of electron–hole pairs (expression (6a)). The PLD/CDW fluctuations are correlated in chain direction on $\xi_\parallel(T)$. $\xi_\parallel(T)$ increases upon cooling below T_{1D} (see Fig. 5 below). Diffraction by 1D PLD fluctuations gives rise to diffuse sheets centered at the $\pm 2k_F$ wave vector in reciprocal space (Fig. 3). The detection of such diffuse sheets, through the formation of $\pm 2k_F$ diffuse lines on X-ray patterns, provided the first observation of the Peierls instability in KCP [11]. Since this pioneering work, X-ray diffuse scattering methods have been widely used to detect PLD fluctuations (mostly by their BOW component) pre-transitional at the Peierls transition in many families of inorganic and organic 1D conductor. For example, Fig. 4 presents X-ray patterns exhibiting this $2k_F$ diffuse scattering at room temperature (RT) in $K_{0.3}MoO_3$ (left part) and $NbSe_3$ (right part).

In the absence of fluctuation, the isolated Peierls chain should undergo a phase transition at the mean-field critical temperature T_P^{MF} defined by expression (23) below. However, 1D thermal fluctuations prevent the establishment of a long-range PLD/CDW order at finite temperature. The observation of a 3D Peierls transition at finite temperature, T_P, which is generally

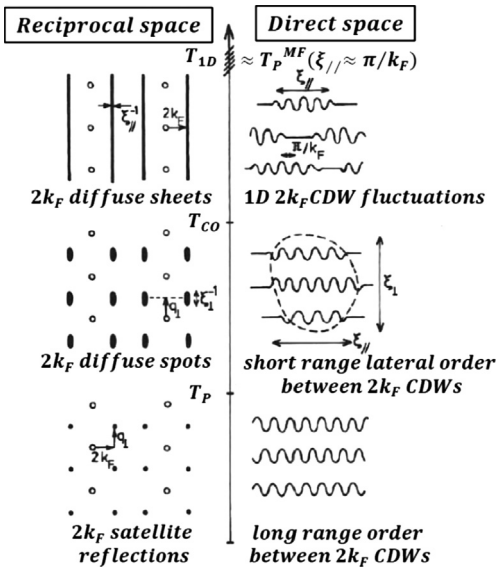

Fig. 3. Diffraction (in reciprocal space – left side) by the $2k_F$ PLD, represented in direct space on the right side, in the 1D fluctuation regime (below T_{1D}), in the inter-chain short range coupling regime (between T_{CO} and T_P) and in the 3D Peierls ground state (below T_P).

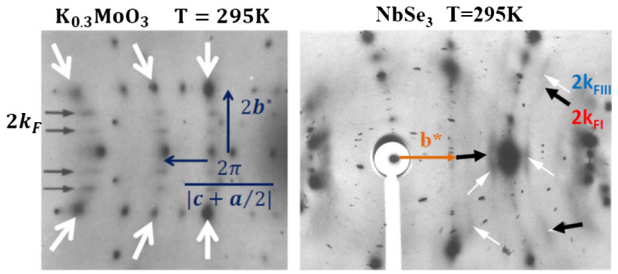

Fig. 4. X-ray patterns from $K_{0.3}MoO_3$ (left) and $NbSe_3$ (right) at RT showing different sets of $2k_F$ diffuse scattering (adapted respectively from Refs. [26] and [27]). Note that the $2k_F$ diffuse segments (black arrows) of $K_{0.3}MoO_3$ perpendicular to the chain direction b are located in broad diffuse lines (white arrows) perpendicular to the $\mathbf{a} + 2\mathbf{c}$ direction and whose origin is commented in the text. In $NbSe_3$ black-and-white arrows show two sets of diffuse lines perpendicular to the chain direction b, which respectively correspond to $2k_F$ fluctuations on type-I and type-III chains defined in Fig. 14b.

Table 1
Bare phonon frequency (Ω_{2k_F}) and nature of the critical phonon mode, mean field (T_P^{MF}) and Peierls (T_P) transition temperatures, Fermi (v_F) and electron–hole pair excitation (v_{eh}) velocities, electron–hole pair coherence length (ξ_o), dimensionless product $\Omega_{2k_F}\tau_{eh}$ (see section 2.3) and type of the Kohn anomaly observed in several families of 1D conductors. T_P^{MF} is calculated from the Peierls gap using the "BCS" relationship (2). T_P^{MF} corresponds also to the temperature T_{1D} at which the $2k_F$ PLD begins to be detected. ξ_o is obtained either from the curvature of the Kohn anomaly (a) or from the high-temperature value of the CDW correlation length $\xi_\parallel$ (b).

1D conductor	Ω_{2k_F} (meV)	T_P^{MF}/T_P (K)	v_F (10^5 m/s)	v_{eh}	ξ_o (Å)	$\Omega_{2k_F}\tau_{eh}$	Kohn anomaly	Ref.
$K_2Pt(CN)_4Br_{0.3}\cdot 3H_2O$	7 (LA)	650/∼100	10	v_F	Large (50?)[a]	0.04	Giant	[33]
$K_{0.3}MoO_3$	7 (mode mixture)	500/180	5.5/1.7 (2 bands)	$\langle v_F \rangle$	18[a,b]	0.04	Phonon softening at T_P	[34]
TTF–**TCNQ** ($2k_F$)	5 (TA)	150/54	1.8	$v_F/7$	6[a,b]	0.17	Incomplete phonon softening at T_P	[35]
TTF–TCNQ ($4k_F$)	8.5 (LA)	600/49	0.9	$v_F/8$	12[b]	1.4	No Kohn anomaly	[36]
$NbSe_3$ ($2k_{FIII}$)	8 (TA/LA)	700/145	2.4	?	13[b]	?	No Kohn anomaly	[37]
$BaVS_3$	5.8 (?)	170/70	4.9	$v_F/10$	7[b]	0.13	Incomplete phonon softening at T_P	[38]

a sizeable fraction of T_P^{MF} (see Table 1), is due to the presence of the inter-chain coupling. The inter-chain coupling manifests below a cross-over temperature T_{CO}, generally close to T_P, by correlating near-neighbor 1D CDW fluctuations on a transverse length $\xi_\perp$. As illustrated in Fig. 3, the anisotropy of these different fluctuations regimes can be clearly distinguished through X-ray diffuse scattering measurements. In the weak electron–phonon coupling limit ($\lambda < 1$), 1D fluctuations begin to be detected around T_P^{MF} when $\xi_\parallel$ amounts to the $2k_F$ PLD wave length.

There are three principal mechanisms of inter-chain coupling:

- the Coulomb coupling between CDW, which will be considered in section 3;
- the transverse nesting of the warped FS due to $t_\perp$. This mechanism is relevant in the temperature range $T < T^* = t_\perp/k_B\pi$ where the thermal broadening of the FS is smaller than $t_\perp$. In that case, the transverse component of the FS nesting wave vector fixes the inter-chain CDW periodicity in the Peierls ground state. Such a mechanism plays a role in the SDW transition of $(TMTST)_2PF_6$, where $T_P = 12$ K $< T^* \sim 100$ K. However, in most of the CDW compounds considered in Table 1 where $T_P > T^*$, the transverse FS nesting process is not relevant.
- the anisotropic dispersion $\hbar\Omega_q$ of the bare phonon branch bearing the $2k_F$ Kohn anomaly for transverse wave vectors $q_\perp$. In that case the minimum of phonon frequency along $q_\perp$ should stabilize the inter-chain PLD periodicity in the Peierls ground state. This effect should be relevant in $K_{0.3}MoO_3$ where the Kohn anomaly develops in a pre-existing valley of soft phonons due to ferroelectric-like fluctuations along the Mo_4O_{21} segment direction shown by red arrows in Fig. 14a (these low frequency phonon modes manifest by the broad X-ray diffuse scattering shown by white arrows in Fig. 4a).

Dynamics of PLD fluctuations is controlled by the bare frequency of the phonon mode Ω_{2k_F} which, when coupled with the electron degrees of freedom of Hamiltonian (3), drives the structural instability of the Peierls transition through the logarithmic divergence of the electron–hole response function $\chi(2k_F, \omega = 0, T)$ – see expression (5). Ω_{2k_F} given in Table 1 is estimated from either the frequency of the critical phonon mode extrapolated at $2k_F$ from frequencies taken outside the dip of the Kohn anomaly (in the adiabatic regime) or from the $2k_F$ phonon frequency when the Kohn anomaly is not really developed above T_P^{MF} or not formed at all (in the anti-adiabatic regime) – see section 2.3. The nature of the regime of PLD/CDW fluctuations depends on the relative value of the bare phonon energy $\hbar\Omega_{2k_F}$ with respect to the mean-field Peierls gap Δ_{MF} given by (1) [28].

In the classical (adiabatic) regime, when $\hbar\Omega_{2k_F} < \Delta_{MF}$, electron–hole pairs are induced by the "quasi-static" $2k_F$ short ranged potential originating from the PLD. When below T_P^{MF} the PLD correlates on $\xi_\parallel$ a local Peierls condensate is formed. The increase of $\xi_\parallel(T)$ upon cooling leads to the progressive development of a pseudo-gap in the one-electron density of states around the Fermi level (see section 2.2). In this case, the pseudo-gap reduces the number of carriers available for charge transport, but also the number of states contributing to the Pauli spin susceptibility. In short, the pseudo-gap achieves a progressive freezing of both charge and spin degrees of freedom.

In the quantum (anti-adiabatic) regime, when $\hbar\Omega_{2k_F} > \Delta_{MF}$, electronic interactions mediated by high-frequency $2k_F$ phonons become non-retarded and attractive. Quantum fluctuations significantly reduce the $T = 0$K PLD and Peierls gap 2Δ [28]. However, the Peierls instability remains present whatever the value of the electron–phonon coupling [29], showing the generality of the Peierls' result. Note that quantum fluctuations have more drastic effect on the Peierls instability in a spin-less electron gas [28,29] and by consequence on the SP instability. In this case, which will be considered in section 2.2, quantum fluctuations can completely destroy the SP gap.

The classical-quantum crossover of the Peierls chain occurs for $\hbar\Omega_{2k_F} \sim \Delta_{MF}$. Experimental Peierls systems are located in the classical/adiabatic regime where, with a soft lattice dynamics, one has $\hbar\Omega_{2k_F} \ll k_B T_P^{MF}$ (see Table 1). Note that the non-observation of a Peierls ground state in the C nanotubes, which are hard materials with $\hbar\Omega_{2k_F} \sim 0.15$ eV $\gg T_P^{MF} \sim 15$ K [30], could be due to the wipe out of Δ by quantum fluctuations. The classical-quantum crossover can be well studied in SP systems (see Fig. 7 below).

For an incommensurate $2k_F$ modulation, the structural order parameter $u(x)$, in quadrature with $\delta\rho(x)$ expressed by (6b) is given by:

$$u(x) = u_0 \sin(2k_F x + \varphi) \tag{8}$$

At finite temperature, the Peierls long-range order of 1D systems is destroyed by thermal fluctuations. These fluctuations are those of the phase φ of the order parameter at low temperature and of its amplitude u_0 at high temperature (see Fig. 5). Due to fluctuations, there is only a short-range order on the correlation length $\xi_\parallel(T)$ on which the 1D order parameter develops. Below we shall label this short-range order parameter by the complex quantity $\hat{u}(x)$. In the adiabatic limit previously defined, the thermodynamics of the 1D fluctuating Peierls chain can be well approximated from the exact solution [31] of the Landau–Ginzburg free-energy functional:

$$F[u] = \int \mathrm{d}x\left[a\left|\hat{u}(x)\right|^2 + b\left|\hat{u}(x)\right|^4 + c\left|\partial\hat{u}(x)/\partial x\right|^2\right] \tag{9}$$

with $= a'(T - T_P^{MF})/T_P^{MF}$; $a(a')$, b and c can be calculated by the microscopic theory of the Peierls transition [18]. Note that the use of a 1D functional assumes that lattice fluctuations associated with the critical phonon mode coupled with fluctuating electron–hole pairs are 1D. This 1D fluctuation regime is assessed by the observation by X-ray diffuse scattering between T_{co} and $T_{1D} \approx T_P^{MF}$ of $2k_F$ diffuse sheets (see Fig. 3).

The thermodynamics of the chain only depends on the extent of the reduced critical region Δt_{1D} defined from the parameters of the functional (9) by:

$$\Delta t_{1D} = \left(b k_B T_P^{MF}\right)^{2/3}/\left(a' c^{1/3}\right) \tag{10}$$

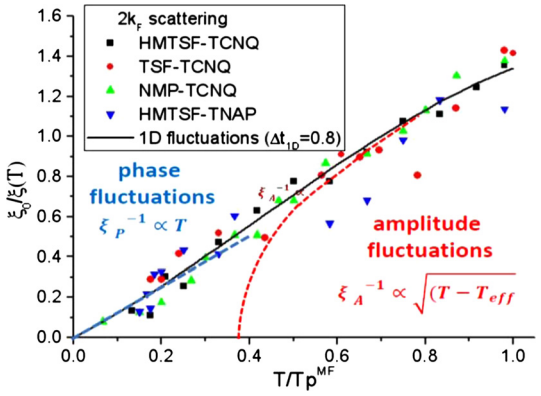

Fig. 5. Thermal dependence of the reduced inverse intra-chain correlation length of 1D incommensurate $2k_F$ PLD fluctuations measured in several organic charge-transfer salts. The continuous line gives the numerical solution of the fluctuating Peierls chain functional (9). The thermal dependence of ξ^{-1} for amplitude and phase fluctuations, respectively relevant at high and low temperatures, is separately shown (adapted from Ref. [32]).

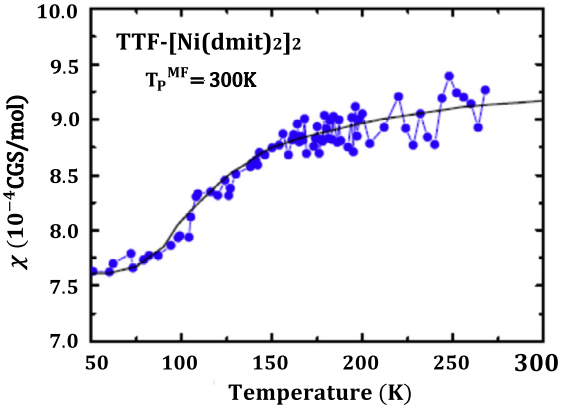

Fig. 6. Thermal dependence of the magnetic susceptibility of TTF–$[Ni(dmit)_2]_2$ (adapted from Ref. [41]). The partial decrease of spin susceptibility corresponds to the complete development of a pseudo-gap in the LUMO conduction band structure of the $Ni(dmit)_2$ stack. The continuous line reports the LRA calculation [39].

For the Peierls chain, one gets $\Delta t_{1D} \approx 0.8$ in unit of T_P^{MF} [18]. Fig. 5 shows that the reduced correlation length $\xi_0/\xi_\parallel(T)$, measured in several organic charge-transfer salts from the half width at half maximum of the $2k_F$ X-ray diffuse sheets [32], follows relatively well the exact solution of the 1D functional (9). In Fig. 5, $\xi_\parallel(T)$ is normalized to the electron–hole thermal coherence length taken at T_P^{MF}:

$$\xi_0 = \hbar v_{eh}/\pi k_B T_P^{MF} \tag{11}$$

where v_{eh} is the velocity of the electron–hole pair excitations considered in section 2.3.

2.2. The pseudo-gap

Fig. 5 shows that the intra-chain correlation length $\xi_\parallel$ of 1D fluctuations of a classical system diverges at 0 K. At this temperature, a true 1D Peierls gap opens at $\sim 2\Delta_{MF}$ (quantum fluctuations are weak in the adiabatic limit). At T finite when $\xi_\parallel$ is finite, the Peierls gap transforms into a pseudo-gap in the density of states whose magnitude and energy dependence is fixed by the length $\xi_\parallel(T)$ on which the local Peierls order is established [39]. Upon cooling from $\sim T_P^{MF}$, the increase in $\xi_\parallel(T)$ leads to a progressive vanishing of the density of states at the Fermi level, $N(E_F)$. Such a vanishing, which involves also the spin degrees of freedom in a free electron gas, can be probed by the decrease of the Pauli spin susceptibility χ_p. This effect was nicely followed by an earlier investigation of KCP using ^{195}Pt Knight shift measurements [40]. Fig. 6 reports a recent measurement of the magnetic susceptibility of TTF–$[Ni(dmit)_2]_2$ [41], which for the first time shows the complete development from $T_P^{MF} \approx 300$ K to $T_P \approx 57$ K of a pseudo-gap in the LUMO (lower unoccupied molecular orbital) conduction band of the $Ni(dmit)_2$ stack. Also the thermal dependence of χ_p quantitatively follows on this temperature range the thermal behavior calculated by Lee, Rice, Anderson (LRA) more than forty years ago [39]. Thus Fig. 6 provides the first complete verification of the LRA theory.

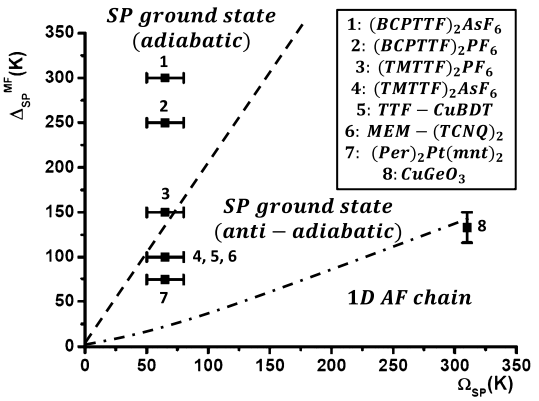

Fig. 7. Nature of the ground state in function of the mean-field SP gap, Δ_{SP}^{MF}, and of the critical phonon frequency Ω_{SP} for the SP Heisenberg chain [44], together with the location of typical SP compounds (adapted from Ref. [45]).

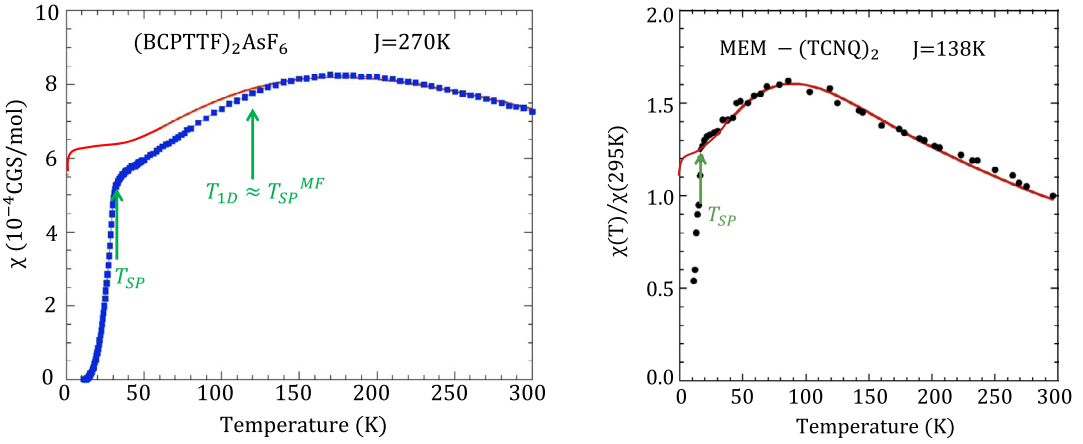

Fig. 8. Thermal dependence of the spin susceptibility of $(BCPTTF)_2AsF_6$ (left) [48] and of the reduced ESR susceptibility of MEM–$(TCNQ)_2$ (right) [49]. The continuous line gives the "exact" thermal dependence of the spin susceptibility of $S = 1/2$ chain with a near-neighbor AF exchange J that is indicated in each figure. T_{SP} is the 30 K/16.5 K 3D SP transition temperature below which a singlet–triple gap of 133 K/–40 K opens in $(BCPTTF)_2AsF_6$/MEM–$(TCNQ)_2$. Note that in $(BCPTTF)_2AsF_6$ the pseudo-gap opens at the onset, T_{1D}, of 1D SP structural fluctuations.

In Heisenberg (XY) AF exchange coupled SP systems the mean-field gap, Δ_{SP}^{MF} is related to the mean-field temperature T_{SP}^{MF} of the SP transition by the correspondence law:

$$\Delta_{SP}^{MF} \approx 2.47 k_B T_{SP}^{MF} \left(1.78 k_B T_{SP}^{MF}\right) \tag{12}$$

Using expression (12) for the Heisenberg AF exchange coupling Δ_{SP}^{MF} can estimated from the temperature $T_{1D} \approx T_{SP}^{MF}$ below which 1D SP structural fluctuations start to develop. Because of the importance of zero-point quantum fluctuations, the singlet–triplet gap measured in the SP ground state is significantly smaller than Δ_{SP}^{MF}. Also the obtaining of Δ_{SP}^{MF} values comparable to the energy of the SP critical phonon Ω_{SP} [42] offers the possibility to study the classical-quantum crossover in the SP phase diagrams established for XY [43] or Heisenberg [44] AF chains. Fig. 7 locates different SP compounds [45] in the phase diagram established for the SP Heisenberg chain [44].

The organic compounds $(BCPTTF)_2AsF_6$ and PF_6 are well inside the classical (adiabatic) phase while MEM–$(TCNQ)_2$ and TTF–CuBDT are in the quantum (anti-adiabatic) phase close to the classical-quantum crossover line $\Delta_{SP}^{MF} \approx 2\hbar\Omega_{SP}$. The organic compounds $Per_2Pt(mnt)_2$ is well inside the quantum phase, while the inorganic compound $CuGeO_3$ is close to the boundary, $\Delta_{SP}^{MF} \approx \hbar\Omega_{SP}/2$, at which the SP gap vanishes. The SP vanishes when the energy of zero-point quantum fluctuations of the critical phonon exceeds the mean-field SP gap.

In the adiabatic limit, SP structural fluctuations lead to the formation of local spin singlets that induce a pseudo-gap in the continuum of excitation of the $S = 1/2$ AF Heisenberg chain. The calculation of the pseudo-gap in the SP Heisenberg chain is however more elaborated than the LRA calculation in the Peierls chain because SP structural fluctuations are magneto-elastically coupled with a spin-less interacting pseudo-fermion gas [46]. The left part of Fig. 8 shows more explicitly that when $\xi_{\parallel}(SP)$ develops below T_{1D} in $(BCPTTF)_2AsF_6$ the growth of a pseudo-gap manifests by a progressive deviation of the experimental spin susceptibility from the one calculated for the uniform $S = 1/2$ chain with a near-neighbor AF exchange J. In the anti-adiabatic limit, SP structural fluctuations does not give rise a pseudo-gap in the continuum of

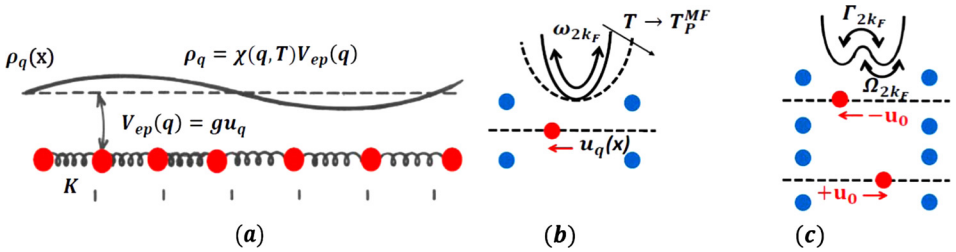

Fig. 9. Left part (a): electron–phonon coupled Peierls chain: the modulation of atomic position (in red), by u_q, leads via the electron–phonon coupling potential $V_{ep}(q)$ to a modulation $\rho(x)$ of the electronic density. $\chi(q,T)$ is the static electron–hole response function of the 1D electron gas. Figures (b) and (c) in the right part give a schematic illustration of the effective potential experienced by the atom (in red) undergoing a PLD with respect to its surrounding (in blue); (b) corresponds to the displacive (adiabatic) limit and (c) to the order–disorder (anti-adiabatic) limit. The characteristic frequencies introduced in the text are also indicated. (For interpretation of the references to color in this figure legend, the reader is referred to the web version of this article.)

excitation. Thus the spin susceptibility of MEM–$(TCNQ)_2$ follows the thermal dependence of the uniform $S = 1/2$ AF chain until the SP transition (right-hand side of Fig. 8). Well inside the quantum phase, the high-frequency critical phonon mode renormalizes the near-neighbor exchange interaction J and adds next near-neighbor exchange components [47] as observed in $CuGeO_3$.

2.3. The Kohn anomaly

While Peierls transitions occur in the classical regime defined by $\hbar\Omega_{2k_F} < \Delta_{MF}$, the various compounds quoted in Table 1 exhibit quite different pre-transitional critical lattice dynamics. This requires the need to define a second adiabatic condition for the formation of a Kohn anomaly. To account for different critical dynamics, we derive in the Appendix the mean-field (RPA) phonon dynamics for a free electron gas weakly coupled with the lattice ($\lambda < 1$).

To introduce the notations let us re-derive the critical phonon dynamics in the adiabatic limit for a weak electron–phonon coupling. One considers, as illustrated in Fig. 9a, an harmonic chain of atoms of mass M linked by the spring constant K_q and coupled with the 1D electron gas by the electron–phonon coupling potential $V_{ep}(q)$.

When one ignores the coupling with the electron gas, the q Fourier component u_q of the atomic displacements follows the harmonic oscillator equation:

$$\ddot{M}u_q + K_q u_q = 0 \tag{13}$$

The mode q corresponds to atomic oscillations with the bare phonon frequency:

$$\Omega_q = \sqrt{\frac{M}{K_q}} \tag{14}$$

Due to the electron–phonon coupling, the atomic displacements submit the electron gas at an "external" potential $V_{ep}(q)$. For a PLD of small amplitude u_0 (typically $u_0 \sim 0.02_5$–0.06 Å for most Peierls systems), the Peierls chain can be treated in the weak electron–phonon coupling limit. In this case $V_{ep}(q)$ can be taken proportional to u_q:

$$V_{ep}(q) = gu_q \tag{15}$$

In (15) g is the electron–phonon coupling constant that we shall take for simplicity to be independent of q. The conduction electrons respond to this external potential by modulating their density. For small $V_{ep}(q)$ in the framework of the linear response theory, the q Fourier component of the charge modulation ρ_q is given by:

$$\rho_q = \chi(q,T)V_{ep}(q) \tag{16}$$

where we use, for Ω_q much smaller than the characteristic frequencies of the dynamics of the electron–hole pairs, the static limit $\omega = 0$ of the electron–hole response function.

The Hamiltonian of coupling between the charge modulation and the electron–phonon potential can be expressed by:

$$H_{ep} = \sum_q \rho_{-q} V_{ep}(q) \tag{17}$$

This Hamiltonian gives rise to a "force" F_q:

$$F_q = \frac{\partial H_{ep}}{\partial u_{-q}} \tag{18}$$

which must be added to the elastic force $K_q u_q$ in the equation of movement (13). The harmonic oscillator equation thus becomes:

$$\ddot{u}_q + \Omega_q^2\left[1 - \frac{2g^2}{K_q}\chi(q,T)\right]u_q = 0 \tag{19}$$

In (19) the electron–phonon coupling renormalizes the bare phonon frequency Ω_q, which thus becomes:

$$\omega(q)^2 = \Omega_q^2\left[1 - \frac{2g^2}{K_q}\chi(q,T)\right] \tag{20}$$

For the critical $2k_F$ wave vector one obtains using expression (5):

$$\omega_{2k_F}(T)^2 = \Omega_{2k_F}^2\left[1 - \lambda\ln\left(\frac{2\gamma\varepsilon_c}{\pi k_B T}\right)\right] = \lambda\Omega_{2k_F}^2\ln\left(\frac{T_P^{MF}}{T}\right) \tag{21}$$

where we have introduced the reduced electron–phonon coupling constant:

$$\lambda = \frac{2g^2}{K_{2k_F}}N(E_F) \tag{22}$$

The weak electron–phonon coupling limit stands for $\lambda < 1$.

The third member of expression (21) involves the mean-field Peierls transition temperature:

$$k_B T_P^{MF} = \frac{2\gamma\varepsilon_c}{\pi}e^{-1/\lambda} \tag{23}$$

T_P^{MF} is the temperature at which the frequency of the Kohn anomaly given by expression (21) in the RPA approximation vanishes. T_P^{MF} is, in absence of thermal fluctuations, the critical temperature of the Peierls transition calculated in the 1950s (see expressions (1) and (2)).

When Ω_q is not negligible with respect to characteristic frequencies of the dynamics of the electron–hole pairs, the ω-dependence of the electron–hole response function must be kept. The equation of movement (19) becomes an explicit equation in ω. In that case, the calculation of the dynamics of the Peierls transition is more elaborated. It is performed in the Appendix using a simplified analytical expression of the electron–hole response function. This calculation allows us to clarify the condition of adiabaticity for the dynamics of the Peierls transition and for the formation of a Kohn anomaly. This condition that controls the nature of the critical phonon dynamics of the Peierls transition relies on a comparison between the frequency of fluctuation of the amplitude of the order parameter, $\omega_A = \sqrt{\lambda}\Omega_{2k_F}$ entering in expression (21) and the lifetime τ_{eh} of the electron–hole pairs at T_P^{MF}, which will be considered below.

The lifetime of the fluctuating electron–hole pairs can be expressed by:

$$\tau_{eh} = \xi_0/v_{eh} \tag{24}$$

In expression (24), ξ_0 is the electron–hole coherence length and v_{eh} is the velocity of the electron–hole pair excitations.

ξ_o given in Table 1 is obtained either from the curvature of the Kohn anomaly if it exists (42) or from the high-temperature ($\sim T_P^{MF}$) value of the CDW correlation length $\xi_{\|}$ (42, 32). v_{eh}, obtained from expression (11), is expressed in Table 1 in fraction of the Fermi velocity v_F, this latter quantity being obtained either from *ab-initio* band calculations or from ARPES measurements.

In the absence of defects, only thermal fluctuations limit the electron–hole pair lifetime. In a free electron gas, one obtains with $v_{eh} = v_F$ in the thermal coherence length ξ_0 given by (11):

$$\tau_{eh} = \hbar v_F/\pi k_B T_P^{MF} = \sqrt{2}\tau_{T_P^{MF}}. \tag{25}$$

The quantity τ_T is used in the Appendix.

In the presence of a potential of defect interrupting the 1D conducting path by introducing a backscattering diffusion process of individual particles, the defects break the pairing (see section 4.3), which reduces the life time τ_{eh}.

In the case of strong (electron–electron or electron–phonon) coupling that tends to localize the electrons, τ_{eh} should be longer than the thermal life time given by expression (25). This is because, due to the carrier localization, the velocity of the electron–hole pair excitations v_{eh} should be smaller than the Fermi velocity v_F, since electrons and holes, dressed by strong electron–electron repulsions or strong (polaron-like) electron–phonon coupling, acquire an enhanced effective mass m_{eff}. If one assumes that v_{eh} is comparable to the effective velocity of each component of the electron–hole pair one should have:

$$m_{eff}v_{eh} \sim mv_F = \hbar k_F \tag{26}$$

Table 1 reports the product $\Omega_{2k_F}\tau_{eh}$ estimated at T_P^{MF} in various families of 1D conductors. As shown in the Appendix, this product governs the nature of the phonon dynamics at the Peierls transition. A well-defined Kohn anomaly is only observed when $\Omega_{2k_F}\tau_{eh} < 1$.

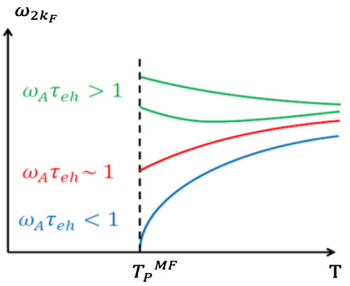

Fig. 10. Mean-field thermal dependence of the $2k_F$ critical phonon frequency, ω_{2k_F}, as a function of the dimensionless quantity $\omega_A\tau_{eh}$ (see Appendix A).

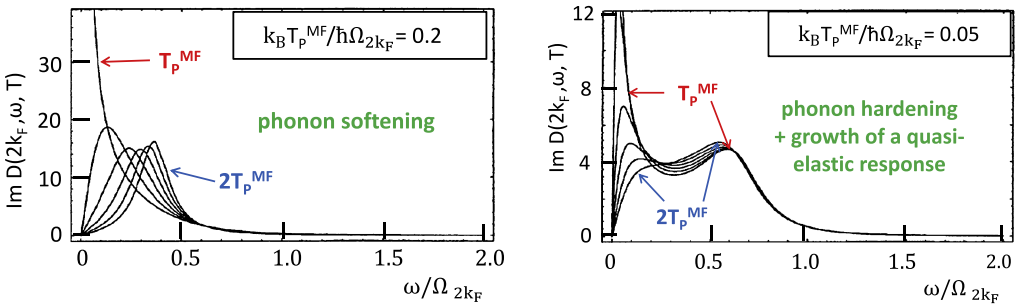

Fig. 11. Imaginary part of the retarded $2k_F$ phonon propagator $\mathrm{Im}\,D(2k_F,\omega,T)$ defined by expression (A.9) of the Appendix for $k_BT_P^{MF}/\hbar\Omega_{2k_F} = 0.2$ (left) and 0.05 (right) as a function of the reduced frequency ω/Ω_{2k_F} [51]. This response is represented between T_P^{MF} and $2T_P^{MF}$ by steps of $0.2T_P^{MF}$.

If $\omega_A\tau_{eh} < 1$, the electron–hole pairs fluctuate so rapidly during the phonon oscillation period that they are able to screen the coupling constant K_q between the atoms. The screening is thus determined by the quasi-static electron–hole response $\chi(2k_F, \omega \approx 0, T)$ which enters in the equation of movement (19). The enhanced q dependence of the response function for $q = 2k_F$ leads to the formation of a Kohn anomaly. At $q = 2k_F$, the phonon frequency $\omega_{2k_F}(T)$, which thus follows the divergence of the electron–hole response function given by expression (5), critically softens upon cooling (see Fig. 10 and the left part of Fig. 11). Upon cooling, the enhanced screening leads to a progressive flattening of the potential, in which the atoms oscillate (Fig. 9b). This drives a lattice instability of displacive type where the deviation of atomic position with respect to their high temperature position, $u(x)$, takes a continuum of values. This generally stabilizes a sinusoidal PLD $u(x)$ in the Peierls ground state. A giant $2k_F$ Kohn anomaly is already formed at RT in the acoustic mode polarized in chain direction of KCP [33]. In the blue bronze $K_{0.3}MoO_3$, the $2k_F$ Kohn anomaly, which progressively softens upon cooling [34], is located in a preexisting soft phonon branch. This branch corresponds to Einstein-like pre-existing soft phonons due to an incipient ferroelectric instability of individual Mo_4O_{21} segments of a 4-corner-sharing octahedron that form the repeat unit of 1D chains (see Fig. 13a). Similar underlying ferroelectric instabilities are found in several others families of 2D metallic oxides and bronzes that are subject to $2k_F$ Peierls-like instabilities [50] (see also the end of this section).

If $\omega_A\tau_{eh} > 1$, the $2k_F$ phonon fluctuates too rapidly during the living time of the electron–hole pairs so that the phonon mode cannot efficiently couple with the electron–hole condensate. There is no screening and thus no critical softening of Ω_{2k_F} when the Peierls transition is approached (Fig. 10). The long-living electron–hole condensate induces via the electron–phonon coupling a quasi-static local $2k_F$ PLD of amplitude u_0 quite well decoupled from the $2k_F$ "critical" phonon. This gives rise above the Peierls transition to a quasi-elastic response in inelastic scattering processes (right-hand part of Fig. 11). The long-time-living structural fluctuations exhibit a Lorentzian-like relaxation (expression (A.13) in the Appendix) whose associated dynamics is typical of an order–disorder transition. Such a dynamics connects, through a double-well potential shown in Fig. 9c, two local atomic deformations $\pm u_0$ or two PLD/CDW cluster configurations, each deformation or configuration achieving a Peierls distortion on a local scale. The change in the conformation of the individual PLD/CDW cluster requires a jump above the potential barrier separating the $\pm u_0$ ground states. This jump process controls the life-time $\tau_{2k_F}(T)$ of individual clusters. The long-range static order stabilized below the Peierls transition is achieved by the critical slowing down of $\tau_{2k_F}(T)$ (together with the divergence of the cluster size $\xi_{\|}(T)$). The slowing down of the dynamics gives rise to a "divergence" of the damping constant $\Gamma_{2k_F}(T)$, defined by expression (A.14), which enters the Lorentzian response (A.13) calculated in the Appendix. The non-detection of a Kohn anomaly associated with the $2k_F$ Peierls instability of $NbSe_3$ [37] and the $4k_F$ instability of TTF–TCNQ [36] suggests the presence of such a relaxation dynamics, which remains to be studied.

Between these previous regimes, one has, by continuity, when $\omega_A\tau_{eh} \sim 1$, an incomplete softening of the frequency of the Kohn anomaly at the Peierls transition (Fig. 10). Such a dynamics is observed in TTF–TCNQ [35] and $BaVS_3$ [38]. In TTF–TCNQ, a weak $2k_F$ Kohn anomaly develops below about 150 K (T_{1D}) in an acoustic branch polarized transversally with respect to the stack direction [35].

In the case of the free electron gas where τ_{eh} is given by (25) and for typical dimensionless electron–phonon coupling constants $\lambda \sim 0.2$–0.4, one founds that the adiabatic–anti-adiabatic crossover condition $\omega_A \tau_{eh} = 1$ occurs (see expression (A.12) of Appendix) for:

$$\left(k_B T_P^{MF}/\hbar\Omega_{2k_F}\right)_c = \frac{\sqrt{\lambda/2}}{\pi} \approx 0.1\text{–}0.14 \quad \text{or} \quad (\Delta_{MF}/\hbar\Omega_{2k_F})_c \approx 0.2\text{–}0.25 \tag{27}$$

This condition agrees with the numerical calculations shown in Fig. 11. Note that the adiabatic condition for the formation of a Kohn anomaly is more restrictive that the one, $\Delta_{MF}/\hbar\Omega_{2k_F} \approx 1$, obtained in section 2.2.

KCP and $K_{0.3}MoO_3$, which both exhibit a well-defined Kohn anomaly, are in the adiabatic limit. Consistently, their $k_B T_P^{MF}/\hbar\Omega_{2k_F}$ ratio is above the critical condition (27). However, for the other 1D conductors quoted in Table 1, whose Peierls dynamics exhibits either the incomplete softening of a Kohn anomaly or a relaxation dynamics, one still obtain a $k_B T_P^{MF}/\hbar\Omega_{2k_F}$ ratio that remains above the condition (27). This means that the quantity τ_{eh} to compare with ω_A should be longer than the thermal life time τ_T obtained for free electrons in the weak electron–phonon coupling limit. Following our previous discussion on the electron–hole life time, this means that the velocity of the electron–hole pair excitations v_{eh} should be smaller than the Fermi velocity v_F. $v_{eh} < v_F$ imply that the electron gas coupled with the lattice is somewhat localized; the localization being due either to strong electron–electron repulsions (case of TTF–TCNQ and $BaVS_3$) or to strong electron–phonon coupling (case of $NbSe_3$).

From the quantitative analysis of the $2k_F/4k_F$ critical X-ray diffuse scattering, v_{eh} estimated in Table 1 for the donor [52] and acceptor [32] stacks of TTF–TCNQ and for $BaVS_3$ [53] are significantly reduced with respect to v_F [54]. The strong reduction of v_{eh} with respect to v_F leads to a $\omega_A \tau_{eh}$ product closer to 1. This can qualitatively explain why only a weak softening is observed for the $2k_F$ Kohn anomaly (on the TCNQ stack) of TTF–TCNQ and of V chain of $BaVS_3$. Also the non-adiabatic dynamics (i.e. absence of Kohn anomaly) of the $4k_F$ CDW instability of TTF–TCNQ is consistent with the observation of a $4k_F$ Wigner-PLD instability on the TTF stack [21,22] of TTF–TCNQ. Note that the presence of sizeable electron–electron repulsions in TTF–TCNQ is assessed by the detection of a pseudo-gap of correlation in infrared conductivity [55].

The dynamics of the Peierls transition calculated in the strong-electron–phonon coupling limit does not exhibit a Kohn anomaly, but a $2k_F$ quasi-static lattice response [56]. The PLD instability consists of the formation of atomic clusters where the displaced atoms form quite well-defined local chemical bonds with their surroundings. In consequence, there is a large gain in energy to achieve the $\pm u_0$ lattice displacement and any deviation of $u(x)$ with respect to these optimal bond distance costs energy. This is consistent with the double-well potential representation shown in Fig. 9c. In each cluster, the atomic displacement $\pm u_0$ should be a sizeable fraction of the interatomic distances. Then the CDW consists of a modulation of the electron occupancy of these well-defined bonds so that the excess or defect of charge of the density wave must be trapped in local atomic clusters. Because of the formation of such atomic clusters, the PLD should be non-sinusoidal. The overall energy gain due to cluster formation relies on a well-defined phasing of the atomic displacements with respect to their surroundings. Thus the PLD, which could incorporate a succession of clusters differing by their relative phase shift, generally forms long-period superstructures. Fluctuations among such trapped configurations are controlled by an order–disorder or relaxation dynamics. Such a dynamics exhibits a critical slowing down of the cluster inverse life time when the Peierls transition is approached from above.

Good examples of such "$2k_F$" PLD and long-period superstructures can be found for $m \geq 7$ in the family of $(PO_2)_4(WO_3)_{2m}$ tungsten bronzes built with a segment of a m-corner-sharing WO_6 octahedron [57]. For example, in the "Peierls" superstructure of the $m = 10$ member, the amplitude of the modulation amounts to $u_0 \sim 0.2$ Å, which represents one tenth of a typical W–O bond distance! [58]. In this superstructure, clusters exhibiting maxima of PLD are made with correlated W displacements principally aligned (i) in a ferroelectric manner in the direction of the segment of the m-octahedron, and (ii) in the opposite (i.e. anti-ferroelectric) manner between neighboring segments. This displacement pattern realizes a good compromise between the "$2k_F$" PLD/CDW instability of the metallic bronze related to its quasi-1D electronic structure and the incipient anti-ferroelectric lattice distortion of the insulating oxide WO_3, which represents the limit of this series when $m \to \infty$.

3. Inter-chain Coulomb coupling between CDWs

As the $2k_F$ PLD modulates the charge density in chain direction, the basic inter-chain coupling mechanism between CDWs is of Coulomb origin. Coulomb coupling of the Madelung type has been calculated by Šaub, Barišić and Friedel (SBF) assuming a linear charge modulation [59]. In the SBF model, the coupling between two CDWs, expressed by (6b), located on chains i and j distant of R_{ij}, and whose origin is shifted by εb, is given by:

$$W_{ij}(2k_F, R_{ij}, \varphi_{i-j}) = \frac{\delta\rho_i \delta\rho_j}{b} \sum_{G \in RR} \cos(\varphi_{i-j} - G\varepsilon b) K_0\left(R_{ij}|2k_F + G|\right) \tag{28}$$

In expression (28) $\delta\rho_i$ and $\delta\rho_j$ are the amplitude of the ith and jth CDWs and φ_{i-j} is their relative phase shift. G is a vector of the reciprocal lattice (RR) of the chain of period b. $K_0(x)$ is the modified zeroth-order Bessel function, which rapidly decays with R_{ij} (x below) as:

$$K_0(x) \sim e^{-x}/\sqrt{x} \tag{29}$$

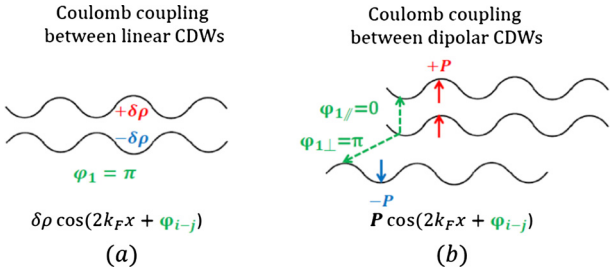

Fig. 12. Coulomb couplings between (a) linear and (b) dipolar CDWs.

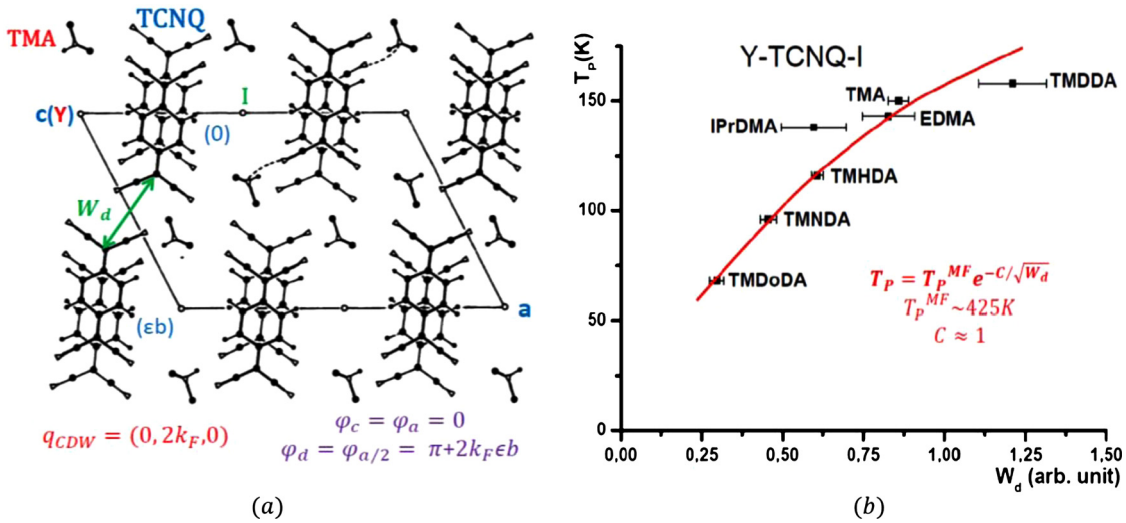

Fig. 13. (a) Structure of TMA–TCNQ-I projected along the stack direction b and transverse phase shift between CDWs located on zigzag-type TCNQ stacks. This figure gives the location of the dominant Coulomb interaction W_d between CDWs (b) 3D Peierls transition temperature T_P in function of W_d calculated in Ref. [60] for the whole Y-TCNQ-I series. The size of the Y^+ cation controls the diagonal coupling W_d through the variation of the lattice parameter c. The continuous line gives T_p calculated in the fluctuation regime of the amplitude of the Peierls order parameter (see expression (30) and Fig. 15).

The exponential spatial decay means that the phase shift φ_{i-j} between CDWs is basically fixed by first-neighbor interactions $|i-j|=1$. Assuming $\varepsilon=0$, $W_{|i-j|}=1$ is minimum for a phase shift of π between first-neighbor chains. This brings an excess of charge, $+\delta\rho$, in regard of a defect of charge, $-\delta\rho$ as shown in Fig. 12a. This CDW's phase shift is observed in the two transverse directions of the Peierls ground state structure of KCP.

In chains made of atomic clusters or of molecules, the CDW is spread on these entities and thus has a lateral extension. Thus one has to go beyond the SBF approximation of a linear charge modulation to calculate the Coulomb coupling. However in many cases, simple arguments based on electrostatic coupling between first-neighbor charged entities can account for the optimal phase shift φ_{i-j}.

In molecular compounds where the CDW modulates the electron occupancy of the LUMO (lower unoccupied molecular orbital) or the hole occupancy of the HOMO (higher occupied molecular orbital) between successive molecules in acceptor or donor stacks respectively, the optimal CDW phase shift results from the minimization of Coulomb interactions between the closest charge distributions in inter-chain directions. This is illustrated by Fig. 13a, giving the optimal phasing in the CDW ground state of the organic TMA–TCNQ-I salt. Here the dominant CDW Coulomb interaction W_d occurs between the cyano groups of neighboring zigzag stacks of TCNQ in regard along the $\mathbf{a}/2+\mathbf{c}$ diagonal direction (note that in this direction the zig-zag TCNQ stacks are shifted by εb).

In inorganic compounds such as the blue bronze, where the $2k_F$ CDW modulates the amplitude of polarization of each linear segment of 4-corner-sharing MoO_6 octahedra forming the chain repeat unit, the inter-chain coupling occurs between the $2k_F$ modulated electric dipoles of the segments. The anisotropy of the electrostatic coupling between polar CDWs in the dipole direction ($\sim \mathbf{a}+2\mathbf{c}$) and in the perpendicular direction $\mathbf{c}^*$, shown in Fig. 12b, explains respectively the uniform and staggered CDW transverse orders (Fig. 14a) found in the Peierls ground state of $K_{0.3}MoO_3$. Coupling between dipolar CDW can also account for the CDW transverse orders observed in $NbSe_3$ (Fig. 14b; see also Ref. [61] for a more complete discussion). In this compound, the dipolar CDWs originate from pairs of strongly coupled type-I or type-III chains in which the individual CDWs primarily order with a π phase shift.

The Ginzburg–Landau formalism introduced in section 2.1 can be generalized to include the inter-chain coupling W. The treatment of the inter-chain coupling term in the mean-field approximation leads a 3D Peierls transition at finite

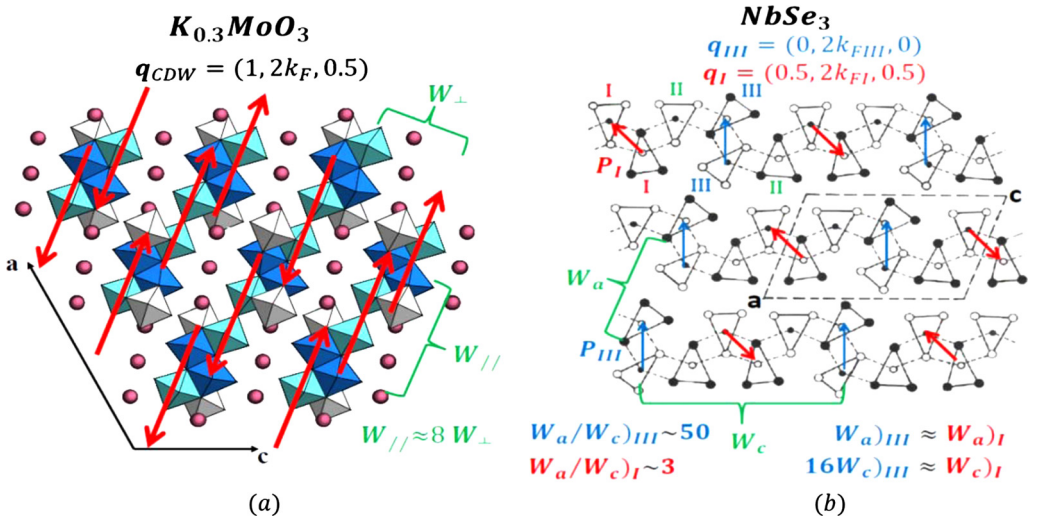

Fig. 14. Structures of $K_{0.3}MoO_3$ (a) and $NbSe_3$(b) projected along the stack direction b. Lateral phasing between the dipolar CDWs in (a) $K_{0.3}MoO_3$ (red arrows) and (b) $NbSe_3$ (red and blue arrows represent dipoles located on pairs of type-I and type-III chains, respectively). The anisotropy of the inter-chain couplings W given in the figure is obtained from the square of the anisotropy of the transverse correlation lengths $\xi_\perp$. (Fig. 14b is adapted from Ref. [61].) (For interpretation of the references to color in this figure legend, the reader is referred to the web version of this article.)

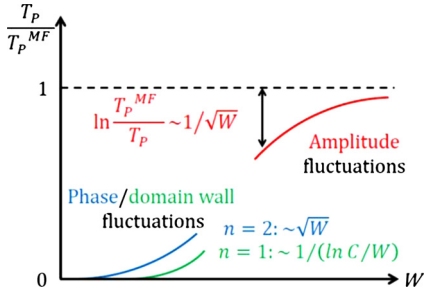

Fig. 15. Variation of T_P scaled to T_P^{MF} as a function of the inter-chain coupling W for the amplitude and phase ($n = 2$)/domain wall ($n = 1$) fluctuation regimes relevant for complex ($n = 2$)/real Ising-type ($n = 1$) order parameters. The variation of T_P with W in the amplitude fluctuation regime is the same for complex- and real-order parameters.

temperature T_P. T_P is an increasing function of the amplitude and correlation length of the 1D fluctuations and of the magnitude of W. The variation of T_P with W, shown in Fig. 15, depends on whether the 3D Peierls transition occurs in the regime of fluctuation of the amplitude or of the phase of the 1D order parameter (see Fig. 5). In the regime of (Gaussian) amplitude fluctuations, one gets [62]:

$$T_P = T_P^{MF} e^{-C/\sqrt{W}} \tag{30}$$

Fig. 13b shows that T_P calculated using expression (30) with W being the dominant W_d inter-chain Coulomb coupling nicely accounts for the variation of the experimental T_P in the Y-TCNQ-I series [60]. As for the Y-TCNQ-I series, Table 1 shows that the T_P of Peierls compounds remains a sizeable fraction of T_P^{MF}.

4. Elasticity, plasticity and pinning of CDW

Below T_P, collective excitations of the 3D PLD sublattice are those of the amplitude and of the phase of the modulation $u(x)$ expressed by (8). The dynamics of the amplitude and of the phase modes of the PLD of $K_{0.3}MoO_3$ have been measured by neutron [34] and X-ray [63] inelastic scatterings, Raman [64] and femtosecond [65] spectroscopies. Phase and amplitude excitations are relatively well decoupled in energy: the amplitude mode is optic-like, while phase excitations are acoustic-like. When $2k_F$ is incommensurate, the vanishing of this acoustic dispersion for $q = 2k_F$ corresponds to the degree of freedom of collective sliding of the phase of the PLD first considered by Fröhlich. For low-energy deformations, the variation of the amplitude of the order parameter can be neglected. In this case, CDW deformations are described by an elastic medium involving continuous long-range deformations of the phase of the PLD for q close to $2k_F$. This assumption is however not valid when large stresses break phase continuity. In that case, plastic deformations nucleate dislocation loops. Also the variation of the amplitude of the order parameter cannot be neglected when large strains, induced for example by strong pinning centers, lead to the formation of Friedel oscillations (FOs).

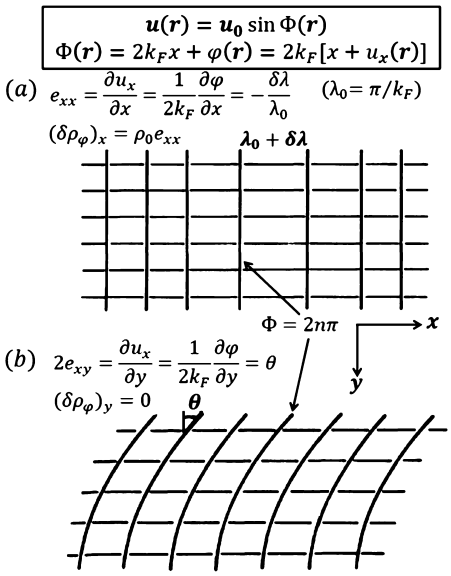

Fig. 16. Two types of deformation of CDWs: (a) compression (dilatation) involves the longitudinal strain e_{xx} and (b) shear involves the strain e_{xy} (adapted from Ref. [66]). The vertical and curved continuous lines in (a) and (b) respectively are surfaces of constant argument Φ.

This section is built on the works by Feinberg and Friedel (F&F), who have first introduced phase elasticity and plasticity of the CDW [66]. They also considered the deformation of the PLD in the presence of various imperfections using local models [67]. Their pioneering work will be illustrated by recent experimental findings.

4.1. CDW phase elasticity

Low-energy deformations are those of the phase $\varphi(\mathbf{r})$ of the PLD modulation defined by expression (8). By analogy with conventional elasticity, F&F have introduced in Refs. [66,67] the elasticity of the phase $\varphi(\mathbf{r})$ of the PLD. Fig. 16 introduces the basic ingredients of the phase elasticity in the case of (a) a compression/dilatation deformation of the PLD and (b) a shear deformation of the PLD.

The compression/dilatation of the phase in the chain direction corresponds to a local change of $2k_F$. Since there are two electrons per 2π CDW period, a phase variation along x induces a modulation of the electronic charge of:

$$\delta\rho(x) = \frac{1}{\pi}\frac{\delta\varphi(\boldsymbol{r})}{\delta x} \tag{31}$$

The charge modulation $\delta\rho(x)$ $(= (\delta\rho_\varphi)_x = \rho_0 e_{xx}$ in Fig. 16a) caused by the deformation along x induces Coulomb forces. If Coulomb forces are dynamically screened by normal carriers excited through the Peierls gap, the compression/dilatation mode is acoustic. In the regime of perfect screening, the acoustic dispersion is governed by the longitudinal elastic constant:

$$K_\varphi^x = \frac{\hbar v_F}{2\pi} \tag{32}$$

If the dynamical screening is not efficient, the longitudinal deformation of the phase induces an optical response. This response corresponds to a plasma frequency $\sqrt{3/2}\omega_A$ due to the rigid displacement of the CDW with respect to the ionic background. Such a regime where the CDW becomes extremely rigid occurs in $K_{0.3}MoO_3$ below ~40 K. Upon cooling $K_{0.3}MoO_3$ from T_P to ~40 K, the reduction in the number of carriers thermally excited through the Peierls gap reduces the screening effect of Coulomb forces induced by the longitudinal phase variation. This causes a sizeable enhancement of the longitudinal elastic constant from the perfectly screened value K_φ^x given by expression (32). This effect has been observed in $K_{0.3}MoO_3$ [68,63].

The shear deformation of the phase along y does not induce any charge redistribution, $(\delta\rho_\varphi)_y = 0$, because $2k_F$ remains unchanged. Thus the dispersion of shear modes, which involves the transverse elastic constant K_φ^y and K_φ^z, remain acoustic whatever the temperature. The elastic constant, K_φ^i, is proportional to the square of the phason acoustic velocity v_φ^i measured in the i direction. Their anisotropy follows also the square of the anisotropy of CDW coherence length ξ_i. The anisotropy of shear deformation elastic constants amounts also to the anisotropy of the inter-chain coupling energy W_i:

$$\frac{K_\varphi^y}{K_\varphi^z} = \left(\frac{v_\varphi^y}{v_\varphi^z}\right)^2 = \left(\frac{\xi_y}{\xi_z}\right)^2 = \frac{W_y}{W_z} \tag{33}$$

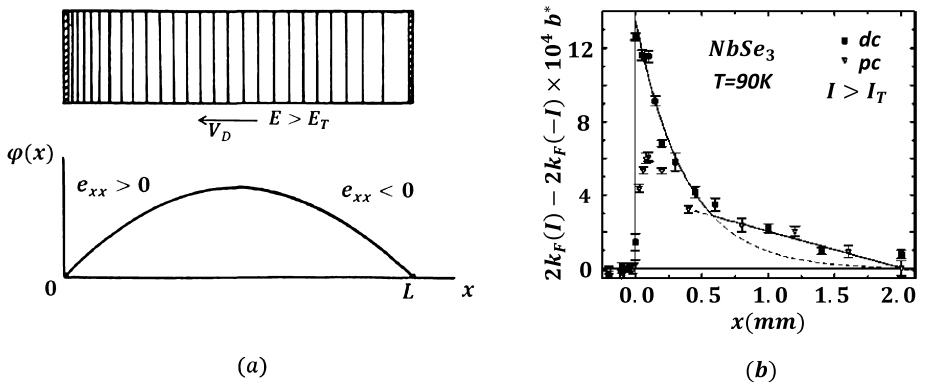

Fig. 17. (a) Elastic longitudinal compression ($e_{xx} > 0$)/dilatation ($e_{xx} < 0$) of the phase $\varphi(x)$ of the CDW submitted to an electric field created by a difference of potential between the electrodes placed on the left and right sides of the sample (x is the chain direction). The continuous lines in the top panel are surfaces of constant argument Φ. The drift velocity, V_D, of sliding CDWs for $E > E_T$ is indicated (adapted from Ref. [66]). (b) Difference of $2k_F(x)$ wave vector under the application of opposite $\pm I$ continuous (dc) and pulse (pc) currents larger than I_T in $NbSe_3$. Note that $2k_F(x)$ varies linearly in the central part of the sample where 0.5 mm $< x <$ 2 mm. Below $x \sim 0.5$ mm, near the current contact located in $x = 0$, it is observed that $2k_F$ decays exponentially with x (this effect is due to the $\pm I$ free-carrier charge conversion into the condensed moving CDW by adding or removing phase wave-fronts). (Adapted from Ref. [71].)

Phason velocities v_φ^i have been measured below T_P along the three principal lattice directions of $K_{0.3}MoO_3$ by inelastic neutron scattering [68]. As expected, their anisotropy follows the anisotropy of the CDW coherence lengths ξ_i of the pre-transitional CDW fluctuations measured above T_P.

An electric field (E) applied in chain direction couples with the local phase φ of the CDW or to the CDW "displacement u_x" defined in Fig. 16. This coupling induces the Fröhlich-type collective sliding of the phase of the electronic CDW accompanied by an oscillating movement of the atomic positions of the PLD. In real systems where the CDW is locally pinned to lattice defects (see section 4.3 below), the collective sliding is only observed when E exceeds a threshold field E_T, as demonstrated in $NbSe_3$ [12] and $K_{0.3}MoO_3$ [13]. In the presence of pinning defects, the competition between elasticity and disorder leads to a generic phase diagram including three dynamical regimes (see for example [69]):

- the creep regime at small electric fields ($E < E_T$), where the CDW is polarized through local phase displacements u_x,
- the CDW de-pinning regime around E_T,
- the collective flow regime for $E > E_T$ when the CDW moves as a whole with a finite velocity V_D.

Figs. 17a and 18 give, in the presence of boundary pinning effects, two illustrations of the CDW elastic response to an external stress caused by the application of a longitudinal electric field E. In these figures, CDW pinning at the electrodes or on sample surface induces respectively a compression/dilatation or a shear deformation of the phase of the CDW.

Fig. 17a illustrates the effect of longitudinal compression ($e_{xx} > 0$) and dilatation ($e_{xx} < 0$) of the phase $\varphi(x)$ resulting from the coupling of CDW with an electric field applied in the chain direction x. The CDW-strain that results has been directly observed using spatially resolved X-ray diffraction measurement of $2k_F(x)$ for sliding CDW in $NbSe_3$ [70,71]. Far from the contact currents, $2k_F(x)$, proportional to $\partial\varphi/\partial x$, varies linearly with x, as predicted by a simple elastic theory; $\varphi(x)$ shown in Fig. 17a has a parabolic dependence on x and vanishes at the electrode positions in $x = 0$ and L. However, this simple picture has to be modified in the blue bronze where it has been surprisingly observed that, above E_T, the $2k_F$ sliding CDW develops an extra-long period modulation in the chain direction, which could be due to the formation of a soliton lattice [72].

Fig. 18 shows that surface pinning leads to a shear deformation of the CDW coupled with an electric field applied in chain direction x. The shear deformation induces a bending of CDW fronts accompanied by a tilt of the $2k_F$ modulation wave vector along y. A shear deformation of the moving CDW along the $2a^*$–c^* weakest inter-layer coupling direction of $K_{0.3}MoO_3$ ($W_\perp$ in Fig. 14a) was first reported more than 30 years ago [73]. Sizeable shear deformations and rotations of the CDW wave vector have been imaged above E_T by monochromatic X-ray topography in ribbon-like $NbSe_3$ presenting pinning surface steps in the chain direction [74]. Recent coherent X-ray diffraction experiments [75] performed below E_T in the creep regime of $NbSe_3$ reveal local shear deformations of the polarized CDW, probably nucleated by domain walls delimiting the more strongly pinned domains where the CDW phase does not move under E. These local shear deformations break the lateral coherence of the CDW sub-lattice.

4.2. CDW dislocation

When the bending angle θ of the shear deformation represented in Fig. 18 exceeds a critical value, the continuity of CDW wave fronts should be broken by nucleation of mixed loop dislocations [66]. For a sliding CDW, the transformation of free carriers into CDW condensed carriers at the electrode implies the creation of new CDW phase wave-fronts. This occurs via a

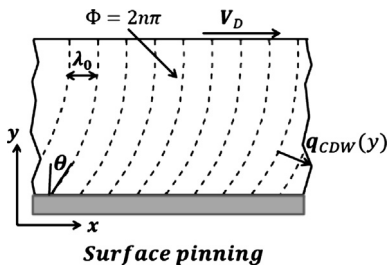

Fig. 18. Shear deformation of a sliding CDW pinned on a surface containing the chain direction. The interrupted curved lines are surfaces of constant argument Φ. The local wave vector $\boldsymbol{q}_{\mathrm{CDW}}(y)$, perpendicular to the bent CDW surface fronts, induces a tilt of $2k_{\mathrm{F}}$ along the transverse direction y. (Adapted from Ref. [67].)

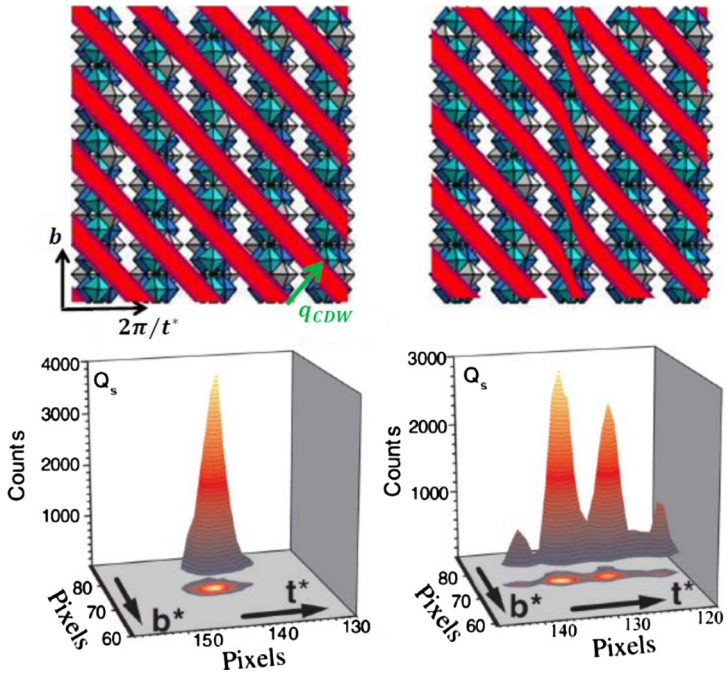

Fig. 19. Regular PLD modulation (left-hand side) and PLD phase dislocation (right-hand side) in $K_{0.3}MoO_3$. The top of the figure gives a representation of the PLD in direct space and the bottom of the figure shows the corresponding diffracted speckle spectra. Because of the tilting of the CDW wave vector $\boldsymbol{q}_{\mathrm{CDW}}$ with respect to chain direction, b, the dislocation mixes edge and screw wave front deformations (from Ref. [77]).

so-called phase slippage phenomenon, which is probably achieved by nucleation and growth of edge loop dislocations [67]. However, it was only recently that an isolated CDW dislocation has been directly imaged using coherent X-ray diffraction in $K_{0.3}MoO_3$ [76] (Fig. 19). The introduction of an abrupt π phase shift in the regular PLD sub-lattice by a dislocation leads to a negative interference term that manifests in the speckle spectra (right side of Fig. 19) by a vanishing of the diffracted intensity at the Bragg position of the regular PLD (left side of Fig. 19). The recent observation of a well-defined multi-peak speckle spectrum in transverse reciprocal direction in the creep regime of $NbSe_3$ [75] shows that the loss of transverse coherence in the CDW sublattice polarized under the application of an electric field should be accompanied by nucleation of CDW dislocations that cause abrupt CDW phase shifts.

4.3. CDW pinning

Non-linear CDW and SDW conductivity phenomena that are observed for $E \geq E_{\mathrm{T}}$ in the density-wave ground state ($T < T_{\mathrm{P}}$) of 1D inorganic and organic conductors such as $NbSe_3$, $K_{0.3}MoO_3$, TTF–TCNQ and $(TMTSF)_2PF_6$ are now well documented [78]. However, the detailed understanding of these electronic phenomena requires a microscopic description of the textured 3D PLD pattern in the presence of pinning centers, a question that is still incompletely settled. The present section reviews the more recent "structural" aspects of this topic.

The delicate question of CDW pinning by randomness begins to be addressed in the 1970s (for a recent review, see [79]). Earlier theories assumed, when the CDW is well developed below T_{P}, that the main effect of the potential defect is to interact with the phase of the PLD/CDW. The most important effect occurs when defects, located on the conducting path,

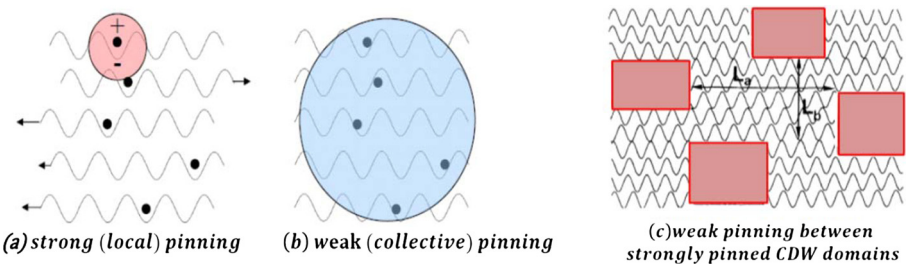

Fig. 20. CDW patterns for strong impurity pinning (a), weak impurity pinning (b) and weak pinning between strongly pinned CDW domains (c). In (a), the arrows show local shears of the CDW lattice due to individual phase adjustments on impurities. In (a) and (b), the dots represent local impurities and in (c) the boxes materialize strongly pinned domains. Parts (a) and (b) are from Ref. [82] and part (c) is from Ref. [84].

strongly perturb the 1D electronic motion. Along a 1D conducting path, the impurity potential induces two scattering processes of the incoming k_F wave function corresponding to the $q \sim 2k_F$ backward scattering process ($k_F \rightarrow -k_F$ reflection of the wave function on the potential barrier; U term below) and to the $q \sim 0$ forward scattering process ($k_F \rightarrow k_F$ transmission of the wave function through the potential barrier; term V below). With the long-range elastic energy term previously considered in section 4.1, the interaction between the phase of the CDW, given by (6b), and disorder potentials (located in m) is described by the Hamiltonian:

$$H_{\varphi\text{-dis.}} = \frac{1}{2}\int \mathrm{d}\boldsymbol{r}\left[K_\varphi^x\left(\frac{\partial\varphi}{\partial x}\right)^2 + K_\varphi^y\left(\frac{\partial\varphi}{\partial y}\right)^2 + K_\varphi^z\left(\frac{\partial\varphi}{\partial z}\right)^2 + \sum_m\left[U\cos\bigl(2k_F x + \varphi(\boldsymbol{r})\bigr)\delta(\boldsymbol{r}-\boldsymbol{r}_m) + V(\boldsymbol{r}-\boldsymbol{r}_m)\frac{1}{\pi}\frac{\partial\varphi}{\partial x}\right]\right] \tag{34}$$

The term U describes the interaction between the impurity and the $2k_F$ oscillating part of the electronic density. The backscattering process causes the individual pinning of $2k_F$ CDW, since the minimization of the cosinus term tends to impose a well-defined phase of the CDW on each impurity site. Such "phase-locking" terms, also present for the PLD, give rise to an asymmetry of intensity between pairs of $+2k_F$ and $-2k_F$ satellite reflections in the diffraction pattern [80]. The backscattering process breaks also the $2k_F$ electron–hole pairing and thus limits the condensate lifetime (see section 2.3). The term V describes the interaction between the impurity and the $q \sim 0$ long-wave-length oscillation of the electronic density given by expression (31). The phase shift that results from the forward scattering process elongates or compresses locally the phase of the CDW (see Fig. 22a below). Concomitant local variations of the phase of the PLD induce an asymmetry of profile of individual $2k_F$ satellite reflections [81].

The U term alone was considered in earlier theories with the effect to pin the phase of the PLD/CDW. As a function of the relative values of the pinning energy gain and of the elastic energy cost, two extreme situations are found:

- when the individual pinning energy gain dominates, the phase of the CDW is adjusted on each impurity site (Fig. 20a). The coherence of the CDW pattern is broken by the randomness of the impurity distribution along both chain and transverse directions (the phase adjustment on impurities induces local shear deformations of the CDW sub-lattice, which also break the optimal inter-chain phasing due to W). In the situation of strong pinning, each CDW coherent domain contains few impurities;
- when the elastic energy cost dominates, there is collective adjustment of the phase of the CDW on the impurity distribution (Fig. 20b). The CDW pattern remains coherent in large domains containing a sizeable number of impurities. In this case the possibility to obtain a Bragg glass with a quasi-long-range CDW order has been considered [83].

The real texture of the pinned CDW pattern is more subtle than those of these two extreme descriptions. In particular, it was suggested on the basis of earlier structural studies of irradiated organic salts [84] that the CDW pattern could be the superimposition of weakly pinned regions, where the phase fluctuates slowly, and strongly pinned domains where the phase is locked (Fig. 20c). In this situation the domain walls play the role of pinning surface as a source of shear deformation of the CDW (see Fig. 18).

The phase of the CDW pinned on an impurity site can be probed by the so-called "white line" effect [80] illustrated in Fig. 21. Such a "white line" effect is revealed by an asymmetry of intensity between pairs of $+2k_F$ and $-2k_F$ satellite reflections in the diffraction pattern from the PLD. This effect, analogous to holography in optics, is due to interference (I_A term) between diffracted beams by impurities (I_{sub}) and by the PLD modulation (I_{dis}) [82]. The "white line" effect observed in solid solutions of organic conductors as well as in substituted inorganic conductor allows one to probe size and/or charge effects of impurities in the pinning process [85]. Using this effect, it has been possible to follow upon heating the thermal de-pinning of the phase of the CDW by thermally excited phasons in doped $K_{0.3}MoO_3$ [86].

Earlier pinning theories ignored local variations of the phase (Fig. 22a) and of the amplitude (Fig. 22b) of the CDW/PLD around impurities. A local variation of the phase, $\delta\varphi(x)$, generally occurs when non-isoelectronic impurities induce a local

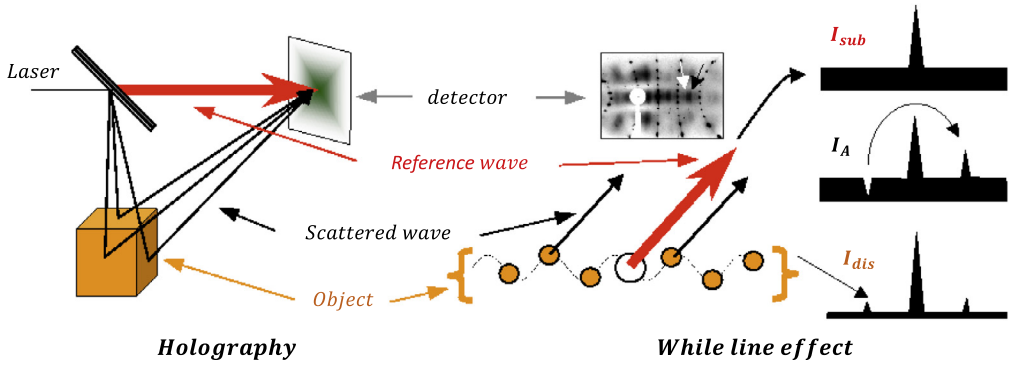

Fig. 21. Schematic representation of the so-called "white line" effect in diffraction and its analogy with holography in optics. (From Ref. [82].)

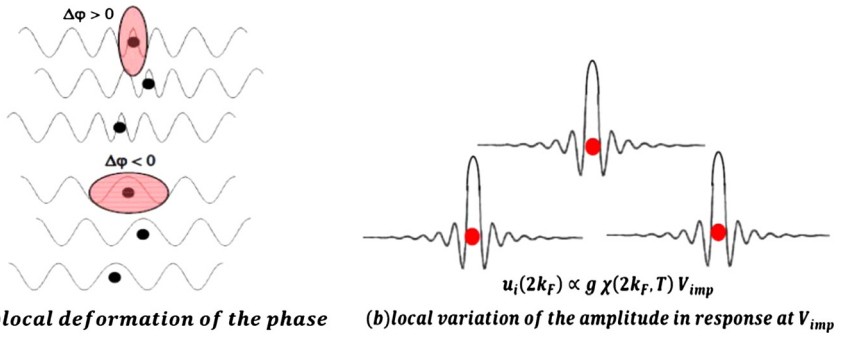

Fig. 22. Local variations of the phase $\Delta\varphi$ (a) and of the amplitude $u_i(2k_F)$ (b) of the CDW around impurity centers (dots). Part (b) represents more specifically the induced 1D FO's of amplitude, $u_i(2k_F)$, in response to the impurity potential V_{imp}.

variation of the charge of the CDW, $\delta\rho(x)$; these two quantities being connected through expression (31). Local variation of the amplitude of the CDW, $u_i(2k_F)$, is expected in response to an impurity potential V_{imp} via the 1D divergent $\chi(q,T)$ electron–hole response function – see Fig. 22b [87]. Both charge screening of non-isoelectronic impurities by a phase shift (not yet considered in the literature until recently [88]) and amplitude [87] variation in response to an impurity potential are the two basic components of Friedel oscillations (FOs). With the same critical $2k_F$ wave vector, 1D FOs should superimpose above T_P to regular 1D $2k_F$ CDW fluctuations and below T_P to the 3D CDW modulation pattern, with however a delicate problem of phase matching between the FOs and the regular CDW that will be considered below.

In response to strong lattice defects, such as those created by X-ray irradiation, 1D FOs can be induced well above $\mathbf{T}_P$. The intensity diffracted by the FOs, which is proportional to the square of the induced PLD $u_i(2k_F)$, defined in Fig. 22b, superimposes on the intensity diffracted by the regular $2k_F$ CDW fluctuations (I_{dis} in Fig. 21). As $|u_i(2k_F)|^2$ is proportional to the square of $\chi(q,T)$, the intensity diffracted by the FOs strongly varies as a function of temperature. This thermal dependence has been measured above T_P in irradiated TMTSF–DMTCNQ [89] and TTF–TCNQ [32] and analyzed in this framework.

Below T_P, the right-hand part of Fig. 23 represents the FOs induced in the vicinity of a V defect in $K_{0.3}MoO_3$ and gives its matching with the regular PLD present at larger distance from the impurity. The structure of the FOs is obtained by a detailed analysis of the high-resolution profile of $\pm 2k_F$ satellite reflections shown in the left-hand part of Fig. 22 [88,86]. A V defect induces both an oscillation of amplitude of the $2k_F$ modulation on few near neighbor Mo sites ($2\xi_\Delta \approx 16$ Å, where $\xi_\Delta = \hbar v_F/2\Delta$ is the damping length in presence of the Peierls gap [87]) and a phase shift $2\eta = -\pi$ on the V site able to screen a difference of charge of one electron ($Z = -1$) with the Mo [90a]. The phase shift is directly related to Z by the Friedel sum rule (see also the contribution by J. Villain, M. Lavagna, and P. Bruno in this issue) because, since in a 1D system the scattered wave is in the same direction as that of the incident one, only the $l = 0$ term enters the Friedel sum rule. This phase shift can be simply understood in 1D since a 2π CDW period contains two electrons, half a CDW period ($-\pi$) is required to screen the impurity charge of one hole. The screening is achieved by a phase variation of the electron density from $+\pi/2$ to $-\pi/2$ on a distance of about one lattice spacing corresponding to the extension of the impurity potential (right-hand part of Fig. 23). However the intra-chain CDW phase shift 2η induces also an inter-chain phase shift of π with neighboring CDWs. This last phase shift cancels the optimal Coulomb inter-chain coupling energy gain, W, in transverse direction (see Fig. 12a in section 3). Thus the best way to recover the optimal inter-chain coupling is to resorb 2η by forming two solitons on each side of the impurity, as shown in the right part of Fig. 23 (each soliton recovering a $-\eta = \pi/2$ half phase shift). The matching of the FOs on the regular PLD by formation of two $\pi/2$ phase shifts could be responsible of the asymmetry of intensity $(-I'_a/+I'_a)$ of the $+2k_F/-2k_F$ reflections observed in the diffraction processes by

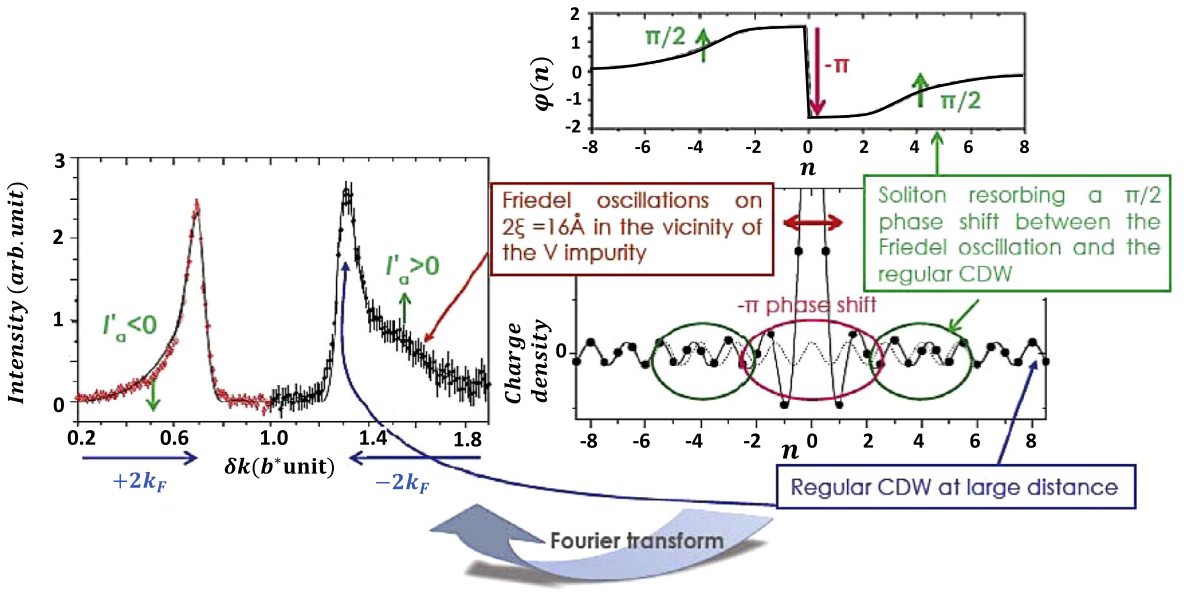

Fig. 23. Right part: FOs with its phase shift of $-\pi$ around a V impurity located at $n = 0$ and its matching with the regular PLD/CDW via the formation of two solitons, each achieving a phase shift of $\pi/2$ at the modulation. The top panel gives the spatial dependence of the phase $\varphi(n)$ of the resulting modulation with respect to the regular PLD/CDW (interrupted lines in the bottom panel). Left part: experimental X-ray diffraction spectrum of $K_{0.3}(Mo_{0.972}V_{0.028})O_3$ at 15 K compared to the Fourier transform (continuous line) of the PLD/CDW modulation shown in the right-hand part. (Adapted from Ref. [88].)

the FOs (see left-hand side of Fig. 23) [90b]. Note also that by the formation of two $\pi/2$ solitons, the total variation of the phase of the CDW perturbed by the impurity, obtained by integration of (31) on the chain length, is zero. This finding means that $\varphi(n)$ should vanish asymptotically on each side of the impurity when $|n|$ becomes large (see the right-hand side of Fig. 23). On large scales, there is thus charge neutrality of defects dressed by the FOs. Thus the spatially averaged $2k_F$ value of the CDW consistently corresponds to $2k_F$ calculated from the 1D band filling obtained by electron count based on chemical formulae of the $K_{0.3}(Mo_{1-x}V_x)O_3$ solid solution: $2k_F(x) = [(3 - 10x)/4]b^*$.

5. Concluding remarks

This review is focused on the CDW/PLD instability in a 1D conductor. It covers mostly the case of the Peierls transition driven by the $2k_F$ divergence of the electron–hole response function. In the presence of strong electron–electron repulsions, the 1D electron–hole response function diverges also for the $4k_F$ critical wave vector, which corresponds to the wave number of a Wigner lattice of localized charges (one localized charge every $1/\rho$ sites) coupled with a PLD [21–23]. These $4k_F$ CDW/PLD effects, which are now well documented in 1D organic compounds, have been reviewed recently [45,91]. They are distinct from the $2k_F$ CDW/PLD Peierls effects that occur in the free-electron gas and that are the main object of this review. Note that for intermediate electron–electron repulsion, the 1D electron gas can exhibit simultaneously $2k_F$ and $4k_F$ electron–hole instabilities [92], as experimentally observed [45,91]. Charge localization effects are also commonly observed in oxides and organic compounds of higher electronic dimensionality. In 1D conductors, the study of quarter-filled systems is particularly interesting because $4k_F$ bond and $4k_F$ site localization phenomena, stabilizing respectively Mott dimer and charge ordered (CO) ground state of different inversion symmetry, are basically decoupled. However, a mixture of bond and charge orders without inversion symmetry can lead to electronic ferroelectricity, as observed in some organic materials [93], and could drive multiferroicity in several classes of materials [94,95].

Another field of current interest concerns the presence of CDW instability in 2D and 3D electronic systems. In 2D layered transition metal oxides and bronzes, where, because of the anisotropic overlap of t_{2g} d-wave functions, the electronic lattice can be decomposed into sub-lattices of differently oriented sets of interpenetrating weakly coupled chains, it is found that PLD/CDW transitions result from a succession of Peierls instabilities driven by the underlying 1D band electronic structure [96,97]. It has also been proposed that the crystal structure of some group V and VI simple elements and A^VB^{VI} compounds could be stabilized by a Peierls-like transition occurring in a prototype 3D cubic lattice, where there is an anisotropic overlap of the p-wave functions (see, for example, [98]). Note that H. Jones was the first to propose in 1934 [4] a similar stabilization mechanism for Bi; see also R.E. Peierls [1] for the column V elements. However, such a mechanism could be questioned [99] if the s–p hybridization which blurs the 1D nature of the orbital overlap cannot be neglected. This is apparently not the case for column-V, -VI and -VII elements, where the s–p hybridization is very small (see the contribution of J.-P. Gaspard in this issue). Incommensurate PLD/CDW modulations are observed in layered transition-metal di-chalcogenides MX_2 [100]. However, the origin of these CDW transitions cannot be simply rationalized by a simple FS nesting mechanism. This leaves

open the possibility of CDW instabilities driven by strong electron–phonon coupling mechanisms. CDW transitions are also observed in 3D electronic systems. For example, three distinct CDW ground states are stabilized below 43 K in $\alpha - U$ (for a recent review, see [101]), with a critical CDW wave vector nesting flat portions of the FS due to narrow f bands [102].

Some 1D systems exhibit complex intertwined orders such a mixt $2k_F$ SDW–CDW in $(TMTSF)_2PF_6$ [19], or even a succession of complex orders combining charge, spin, orbitals and lattice degrees of freedom as found in the t_{2g} multiband $BaVS_3$ compound [53]. Complex spin, charge and orbital current modulations are also observed in 2D superconducting cuprates. However, the wide panel of denominations used to describe the charge effects (CDW, CO, d-wave bond order, charge and spin stripes, charge "nematicity", etc.) together with the presence in most of the compounds of a meso-/nano-scale phase separation show that a clear physical picture is far to emerge (for recent reviews, see [103,104]).

CDW, SDW, orbital anti-ferromagnetism and spin currents ground states are predicted when semi-conductors/semi-metals with small indirect bandgap/overlap exhibit an excitonic instability [105]. In these transitions towards an excitonic insulator, the mechanism appears to be similar to that of the Peierls transition, the wave vector **Q** that links the energy extremes of the hole and electron pockets playing the same role as the $2k_F$ nesting wave vector of a 1D Fermi surface. Good candidates for such transitions could be the incompletely nested semi-metallic oxides and bronzes [97].

The phase diagram of many density-wave (CDW, SDW, CO) systems includes also superconductivity. In most of them, superconductivity develops under pressure at the vanishing point of the density-wave ground state. This situation is well illustrated by organic conductors [106,107]; see also the contribution of D. Jérome in this issue. However, in multiband conductors or when Fermi level states of a single-band conductor are not completely removed by the nesting process, superconductivity could coexist with the CDW modulation. Coexistence between CDW and superconductivity is observed in cuprates, in 1T–$TiSe_2$ and in the multiband charge transfer organic conductor $TTF[Ni(dmit)_2]_2$ (see [41] and earlier references therein).

6. Chemical index

BCPTTF: benzocyclopenthyl-tetrathiafulvalene
CuBDT: bis-dithiolate copper
dmit: isotrithione-dithiolate
KCP: $K_2Pt(CN)_4Br_{0.3}\cdot 3H_2O$
MEM: *N*-methyl-*N*-ethylmorpholinium
mnt: maleonitrile-dithiolate
Per: perylene
TCNQ: 7,7,8,8-tetracyano-*p*-quinodimethane
TMA: trimethyl-ammonuim
TMTSF: tetramethyl-tetraselenafulvalene
TMTTF: tetramethyl-tetrathiafulvalene
TTF: tetrathiafulvalene

Acknowledgements

This paper is written in memory of Prof. Jacques Friedel who has always considered the physics of low-dimensional conductors as resulting from a subtle interplay between electronic and structural degrees of freedom. The author recognizes more than 40 years of live discussions with him on that topic. Here I want to especially acknowledge our last discussions concerning the history of the Peierls transition. The part on phonon dynamics of the Peierls transition is built on discussions with the late H.J. Schulz. Several results quoted in this review have been obtained in collaboration with C. Coulon, P. Foury-Leylekian, C. Pasquier, and S. Ravy. Finally, this paper has also benefited of fruitful discussions with C. Bourbonnais, V. Jacques, D. Leboloc'h, and G. Montambaux. The author is also very grateful to H. Bouchiat and J. Villain for their comments on the manuscript.

Appendix A. Mean-field dynamics of the Peierls transition

Inelastic neutron scattering by phonons measures the ω Fourier transform $S(q,\omega)$ of the time-dependent displacement–displacement correlation function $\langle u_q(t)u_{-q}(0)\rangle$, which can be expressed as:

$$S(q,\omega,T) = \coth\left(\frac{\hbar\omega(q)}{2k_BT}\right)\mathrm{Im}\,D(q,\omega,T) \tag{A.1}$$

In (A.1) $\coth(x)$ is the Bose–Einstein occupation number of the $\omega(q)$ phonon branch and $D(q,\omega,T)$ is the phonon propagator. For the electron–phonon coupled system considered in Fig. 9a, $D(q,\omega,T)$ is expressed by the Dyson equation:

$$D(q,\omega,T) = \frac{2\Omega_q}{\omega^2 - \Omega_q^2 - 2\Omega_q\tilde{g}^2\chi(q,\omega,T)} \tag{A.2}$$

Note that expression (A.2) involves the electron–phonon coupling constant $\tilde{g}$, which is related to the term g introduced in section 2.3 by the relationship:

$$\tilde{g} = g\sqrt{\Omega_q / K_q}$$

For a linearized electronic dispersion of the 1D electron gas, the $2k_F$ Lindhard electron–hole response function can be expressed under the compact form [18]:

$$\chi(2k_F, \omega, T) = N(E_F)\left[\ln\left(\frac{2\gamma\varepsilon_c}{\pi k_B T}\right) + \psi\left(\frac{1}{2}\right) - \psi\left(\frac{1}{2} - i\frac{\hbar\omega}{4\pi k_B T}\right)\right] \tag{A.3}$$

In (A.3), $\psi(z)$ is the digamma function. $\psi(z)$ is the sum of real and imaginary components, which are respectively even and odd in frequency. Thus (A.3) can be generally written as:

$$\chi(2k_F, \omega, T) = N(E_F)\left[\ln\left(\frac{2\gamma\varepsilon_c}{\pi k_B T}\right) - \Sigma\left(\omega^2, T\right) + i\omega\tau\left(\omega^2, T\right)\right]. \tag{A.4}$$

For $\hbar\omega < 4\pi k_B T$, one has the development:

$$\Sigma\left(\omega^2, T\right) \approx \omega^2\tau_T^2, \tag{A.5a}$$

$$\tau\left(\omega^2, T\right) \approx \tau_T'\left(1 - \frac{\omega^2\tau_T'^2}{8}\right), \tag{A.5b}$$

with:

$$\tau_T = \xi_T / v_F = \hbar/\sqrt{2}\pi k_B T, \quad \text{and} \quad \tau_T' = 1.75\tau_T.$$

$D(q, \omega, T)$ can thus be written in the general form:

$$D(2k_F, \omega, T) = \frac{2\Omega_{2k_F}}{\omega^2 - \omega_R(\omega^2, T)^2 + i\omega\Gamma(\omega^2, T)} \tag{A.6}$$

Expression (A.6) explicitly involves with the notations of (A.4):

– the renormalized square phonon frequency $\omega_R\left(\omega^2, T\right)^2 = \omega_A^2\left[\ln\left(\frac{T_P^{MF}}{T}\right) - \Sigma\left(\omega^2, T\right)\right]$ (A.7)

– the damping $\Gamma\left(\omega^2, T\right) = \omega_A^2\tau\left(\omega^2, T\right)$ (A.8)

In these expressions $\omega_A = \sqrt{\lambda}\Omega_{2k_F}$ is the frequency of the amplitude mode, $\lambda = 2\tilde{g}^2 N(E_F)/\Omega_{2k_F}$ is the dimensionless electron–phonon coupling constant (see also expression (22)) and T_P^{MF} is given by expression (23).

Neutron scattering measures the imaginary part of (A.6):

$$\mathrm{Im}\, D(2k_F, \omega, T) = \frac{2\Omega_{2k_F}\omega\Gamma(\omega^2, T)}{[\omega^2 - \omega_R(\omega^2, T)^2]^2 + \omega^2\Gamma(\omega^2, T)^2} \tag{A.9}$$

Poles of (A.9) give the dynamics of the $2k_F$ critical phonon. When the damping can be neglected, the frequency of the soft phonon $\omega_{2k_F}(T)$ is the solution of the implicit equation:

$$\left(\frac{\omega}{\omega_A}\right)^2 = \ln\left(\frac{T}{T_P^{MF}}\right) + \Sigma\left(\omega^2, T\right) \tag{A.10}$$

This equation is graphically solved in Fig. 24.

If $\omega_A\tau_T < 1$, the intersection between the left-hand-side and right-hand-side members of (A.10) gives the frequency $\omega_{2k_F}(T)$ of the Kohn anomaly renormalized by electron–phonon coupling. Its frequency is smaller than Ω_{2k_F}. Furthermore, when T tends to T_P^{MF}, $\omega_{2k_F}(T)$ softens according to expression (21) of section 2.3:

$$\omega_{2k_F}(T) = \omega_A \ln\left(\frac{T}{T_P^{MF}}\right) \tag{A.11}$$

This situation, which corresponds to the adiabatic limit, is depicted by the numerical simulation of the left-hand part of Fig. 11. Note that when $\omega_{2k_F}(T)$ tends to zero, one has to include the thermally-dependent damping term $\Gamma(\omega^2, T)$ in the phonon-softening mechanism. There are also non-harmonic corrections included in the free energy (9), which are ignored in the RPA approximation. They will be considered at the end of the Appendix.

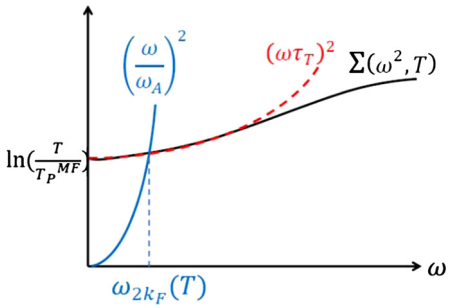

Fig. 24. Graphical solution $\omega_{2k_F}(T)$ of the implicit equation (A.10).

If $\omega_A\tau_T > 1$, the intersection occurs at frequencies close to Ω_{2k_F}. The (weakly) renormalized frequency ω_{2k_F} is determined by the behavior of $\Sigma(\omega^2, T)$ at large values of ω. There is no phonon softening. This situation corresponds to the anti-adiabatic limit.

An incomplete phonon softening occurs when $\omega_A\tau_T \sim 1$. To analyze this behavior, one must take into account the thermal dependence of τ_T through the critical dimensionless quantity $\omega_A\tau_T$ which can be written under the form:

$$\omega_A\tau_T = \left(\frac{T_P^{MF}}{\Omega_{2k_F}}\right)_c \frac{\Omega_{2k_F}}{T} \tag{A.12}$$

In (A.12) the critical ratio $(k_B T_P^{MF}/\hbar\Omega_{2k_F})_c$ amounts to $\frac{\sqrt{\lambda/2}}{\pi} \approx 0.1$–$0.14$. When the temperature decreases towards T_P^{MF}, (A.12) increases. When for $T > T_P^{MF}$, T/Ω_{2k_F} becomes larger than the critical ratio $(T_P^{MF}/\Omega_{2k_F})_c$ a phonon hardening, shown in Fig. 11b, results from the increase of the $\Sigma(\omega^2, T)$ term upon cooling. However, it is also possible to have a high-temperature phonon softening, when $\omega_A\tau_T < 1$, which however never vanish if, when T approaches T_P^{MF}, $\omega_A\tau_T$ becomes larger than 1. Also by continuity, a phonon softening at high temperature could be followed by phonon hardening near T_P^{MF}. Fig. 10 illustrates these different behaviors. Note that the longitudinal acoustic branch of TTF–TCNQ exhibits a frequency hardening around the $4k_F$ critical wave vector upon cooling [36].

The right-hand part of Fig. 11 shows in the non-adiabatic regime that, in addition to the phonon hardening phenomenon previously discussed, $\mathrm{Im}\, D(2k_F, \omega, T)$ exhibits a quasi-elastic response that critically narrows in frequency when T_P^{MF} is approached. To calculate this quasi-elastic response, one must consider on the same footing the low-frequency dependence of $\Sigma(\omega^2, T)$ and of the damping term $\Gamma(\omega^2, T)$ given by expressions (A.5). In the lowest order in ω, (A.9) becomes a Lorentzian response:

$$\mathrm{Im}\, D(2k_F, \omega, T) \sim \frac{\text{constant}}{\omega^2 + \Gamma_{2k_F}(T)^2} \tag{A.13}$$

The frequency dependence of (A.13) is typical of a relaxation dynamics. Furthermore, the damping constant $\Gamma_{2k_F}(T)$ of the Lorentzian response critically decreases to T_P^{MF} according to:

$$\Gamma_{2k_F}(T) = \frac{\ln(\frac{T}{T_P^{MF}})}{\tau'_{T_P^{MF}}} \tag{A.14}$$

The mean-field theory of the dynamics of the SP transition gives a critical ratio $(k_B T_{SP}^{MF}/\hbar\Omega_{SP})_c \approx 0.45$ or $\hbar\Omega_{SP} \approx \Delta_{SP}^{MF}$, significantly larger than the one found for the Peierls chain (expressions (27) and (A.12)). This critical ratio separates adiabatic and anti-adiabatic fluctuations regimes (see [108] and Fig. 4 in Ref. [42]).

Non-harmonic terms are relevant to describe the true dynamics of the Peierls chain beyond the RPA approximation [109]. When for $\omega_A\tau_T < 1$, the dynamics includes these terms, the Kohn anomaly tends to soften at $T_{eff} \sim 0.38 T_P^{MF}$ defined in Fig. 5. However, because of sizeable 1D fluctuations, the Kohn anomaly becomes over-damped around T_{eff}. Below T_{eff}, when the Peierls order is established on a large correlation length $\xi_{\|}(T)$, the damping diminishes and one recovers a dynamics of decoupled fluctuations of the amplitude and of the phase of the order parameter. There is no real softening and thus no true Peierls transition for an isolated Peierls chain at finite temperature in agreement with thermodynamics arguments. The dynamics of the Peierls systems quoted in Table 1 is in fact measured in real systems made of coupled chains. When T_P is comparable to or larger than T_{eff}, pre-transitional Peierls dynamics basically follow that given by the mean-field theory with T_P replacing T_P^{MF}. This is the case of the Kohn anomaly measured in $K_{0.3}MoO_3$ where $T_P \sim T_{eff}$. However, in this compound, the amplitude mode fluctuations already emerge from the damped Kohn anomaly at a frequency comparable to ω_A above T_P [110].

References

[1] R.E. Peierls, Quantum Theory of Solids, Oxford University Press, London, 1955, p. 108. This book is issued from lectures given at Les Houches summer school in 1953. The electronic energy gain due to the setting of a PLD is mentioned in the lecture notes, while the stability of the modulated ground state is only briefly evoked in the book. This work is commented by his author in R. Peierls, More Surprises in Theoretical Physics, vol. 19, Princeton Series in Physics, Princeton University Press, 1991, section 2.3, pp. 27–30.
[2] H. Fröhlich, Proc. R. Soc. Lond. Ser. A, Math. Phys. Sci. 223 (1954) 296.
[3] J. Friedel, Phase change and electron–phonon coupling in perfect crystals. Modulated structures: an introduction, in: T. Riste (Ed.), Electron–Phonon Interactions and Phase Transitions, in: NATO ASI B, vol. 29, Plenum Press, New York, 1977, pp. 1–49.
[4] H. Jones, Proc. R. Soc. 144 (1934) 225;
H. Jones, Proc. R. Soc. 147 (1934) 396;
see also N.F. Mott, H. Jones, Theory of Properties of Metals and Alloys, Oxford, UK, 1936.
[5] R.E. Peierls, Ann. Phys. 4 (1930) 121.
[6] C.G. Kuiper, Proc. R. Soc. Lond. Ser. A, Math. Phys. Sci. 227 (1955) 214.
[7] C.G. Kuiper, Adv. Phys. 8 (1959) 1.
[8] D.C. Mattis, W.D. Langer, Phys. Rev. Lett. 25 (1970) 376;
D.C. Mattis, J. Phys., Colloq. 32 (1971) C1-1086.
[9] M.J. Rice, S. Strässler, Solid State Commun. 13 (1973) 12.
[10] A.W. Overhauser, Phys. Rev. 167 (1968) 691.
[11] R. Comès, H. Launois, M. Lambert, H.R. Zeller, Phys. Rev. B 8 (1973) 571.
[12] P. Monceau, N.P. Ong, A. Portis, A. Meerschaut, J. Rouxel, Phys. Rev. Lett. 37 (1976) 602.
[13] J. Dumas, C. Schlenker, J. Marcus, R. Buder, Phys. Rev. Lett. 50 (1983) 757.
[14] J.C. Slater, Phys. Rev. 82 (1951) 538.
[15] A.W. Overhauser, Phys. Rev. Lett. 4 (1960) 462.
[16] J. des Cloizeaux, J. Phys. Radium 20 (1959) 606.
[17] W.M. Lomer, Proc. Phys. Soc. 80 (1962) 489.
[18] D. Jérome, H.J. Schulz, Adv. Phys. 31 (1982) 299.
[19] J.-P. Pouget, S. Ravy, J. Phys. I 6 (1996) 1501;
J.-P. Pouget, S. Ravy, Synth. Met. 85 (1997) 1523.
[20] A.W. Overhauser, Phys. Rev. B 29 (1984) 7023.
[21] J.P. Pouget, S.K. Khanna, F. Denoyer, R. Comès, A.F. Garito, A.J. Heeger, Phys. Rev. Lett. 37 (1976) 437.
[22] J. Kondo, K. Yamaji, J. Phys. Soc. Jpn. 43 (1977) 424;
J. Hubbard, Phys. Rev. B 17 (1978) 494.
[23] Here we use the general denomination of Wigner lattice although different regimes of charge localization occur in function of the magnitude of the long range Coulomb potential and of the electron density per site ρ – see B. Valuenzuela, S. Fratini, D. Baeriswyl, Phys. Rev. B 68 (2003) 045112. The $4k_F$ modulation observed in TTF–TCNQ [21] corresponds to the small amplitude $4k_F$ CDW regime.
[24] P. Pincus, Solid State Commun. 9 (1971) 1971.
[25] M.C. Cross, D.S. Fischer, Phys. Rev. B 19 (1979) 402.
[26] J.-P. Pouget, S. Kagoshima, C. Schlenker, J. Marcus, J. Phys. Chem. Lett. 44 (1983) L113.
[27] J.-P. Pouget, R. Moret, A. Meerchaud, L. Guemas, J. Rouxel, J. Phys., Colloq. 44 (1983) C3-1729.
[28] L.G. Caron, C. Bourbonnais, Phys. Rev. B 29 (1984) 4230;
H. Bakrim, C. Bourbonnais, Phys. Rev. B 76 (2007) 195115.
[29] J.E. Hirsch, E. Fradkin, Phys. Rev. Lett. 49 (1982) 402.
[30] A. Sédéki, L.G. Caron, C. Bourbonnais, Phys. Rev. B 62 (2000) 6975.
[31] D.J. Scalapino, M. Sears, R.A. Ferell, Phys. Rev. B 6 (1972) 3409.
[32] J.-P. Pouget, Z. Kristallogr. 219 (2004) 711.
[33] B. Renker, H. Rietschel, L. Pintschovius, W. Gläser, P. Brüesch, D. Kuse, M.J. Rice, Phys. Rev. Lett. 30 (1973) 1144;
R. Comès, B. Renker, L. Pintschovius, R. Currat, W. Gläser, G. Scheiber, Phys. Status Solidi B 71 (1975) 171.
[34] J.-P. Pouget, B. Hennion, C. Escribe-Filippini, M. Sato, Phys. Rev. B 43 (1991) 8421.
[35] G. Shirane, S.M. Shapiro, R. Comès, A.F. Garito, A.J. Heeger, Phys. Rev. B 14 (1976) 2325.
[36] J.-P. Pouget, S.M. Shapiro, G. Shirane, A.F. Garito, A.J. Heeger, Phys. Rev. B 19 (1979) 1792.
[37] H. Requardt, J.E. Lorenzo, P. Monceau, M. Krisch, Phys. Rev. B 66 (2002) 214303.
[38] Y. Tanaka, J. Sutter, A. Baron, S. Tsutsui, H. Nakamura, Spring-8 experimental report 2005A0157-ND3d, p. 160 (unpublished).
[39] P.A. Lee, T.M. Rice, P.W. Anderson, Phys. Rev. Lett. 31 (1973) 462.
[40] H. Niedoba, H. Launois, O. Brinkmann, H.U. Keller, J. Phys. Lett. Paris 35 (1974) L251.
[41] W. Kaddour, M. Monteverde, P. Auban-Senzier, H. Raffy, J.-P. Pouget, C.R. Pasquier, P. Alemany, E. Canadell, L. Valade, Phys. Rev. B 90 (2014) 205132.
[42] J.-P. Pouget, Eur. Phys. J. B 20 (2001) 321;
J.-P. Pouget, Eur. Phys. J. B 24 (2001) 415.
[43] L.G. Caron, S. Moukouri, Phys. Rev. Lett. 76 (1996) 4050.
[44] R. Citro, E. Orignac, T. Giamarchi, Phys. Rev. B 72 (2005) 024434.
[45] J.-P. Pouget, Physica B 407 (2012) 1762.
[46] B. Dumoulin, C. Bourbonnais, S. Ravy, J.-P. Pouget, C. Coulon, Phys. Rev. Lett. 76 (1996) 1360.
[47] K. Kukobi, H. Fukuyama, J. Phys. Soc. Jpn. 56 (1987) 3126.
[48] C. Coulon, personal communication, 2005. A comparison of earlier measurements with the calculation of the thermal dependence of the SP pseudo-gap can be found in Ref. [46].
[49] C. Coulon, personal communication, 1990.
[50] P. Foury-Leylekian, J.-P. Pouget, Solid State Sci. 4 (2002) 387.
[51] H.J. Schulz, personal communication (1997).
[52] B. Dumoulin, J.-P. Pouget, C. Bourbonnais, Synth. Met. 103 (1999) 1797.
[53] P. Foury-Leylekian, P. Leinenger, V. Ilakovac, Y. Joly, S. Bernu, S. Fagot, J.-P. Pouget, Physica B 407 (2012) 1692.
[54] For a Luttinger liquid of charge and spin velocities, v_ρ and v_σ respectively, the velocity of the $2k_F$ electron–hole pair excitations is $v_{eh} = \sqrt{v_\rho v_\sigma}$ and the velocity of the $4k_F$ electron–hole pair excitations is $v_{eh} = v_\rho$ (L. Dumoulin, Thesis, Université de Sherbrooke, Canada, 1997). Theory of the pure Luttinger liquid gives v_ρ larger than v_F. However, a strong decrease in the collective velocity of charge fluctuations is found in presence of electron–phonon backscattering of momentum transfer $\sim 2k_F$ (J. Voit, H.J. Schulz, Phys. Rev. B 37 (1988) 10068). This goes with an enhancement of the tendency to form a CDW state in presence of this electron–phonon coupling.

[55] C.S. Jacobsen, I. Johanssen, K. Bechgaard, Phys. Rev. Lett. 53 (1984) 194.
[56] S. Aubry, P. Quemerais, Breaking of analyticity in charge density wave systems: physical interpretation and consequences, in: C. Schlenker (Ed.), Low-Dimensional Electronic Properties of Molybdenum Bronzes and Oxides, Kluwer Acad. Publ., Dordrecht, 1989, pp. 295–405.
[57] A. Ottolenghi, J.-P. Pouget, J. Phys. I 6 (1996) 1059.
[58] P. Roussel, P. Labbé, H. Deligny, D. Groult, P. Foury-Leylekian, J.-P. Pouget, Phys. Rev. B 62 (2000) 176.
[59] K. Šaub, S. Barišić, J. Friedel, Phys. Lett. 56A (1976) 302.
[60] C. Coulon, S. Flandrois, P. Delhaes, C. Hauw, P. Dupuis, Phys. Rev. B 23 (1981) 2850.
[61] S. Rouzière, S. Ravy, J.-P. Pouget, R.E. Thorne, Solid State Commun. 97 (1996) 1073.
[62] H.J. Schulz, The crossover from one to three dimensions: Peierls and spin-Peierls instabilities, in: D. Jérome, L.G. Caron (Eds.), Low-Dimensional Conductors and Superconductors, in: NATO ASI Ser., Ser. B: Phys., vol. 155, Plenum Press, New York, 1987, pp. 95–112.
[63] S. Ravy, H. Requardt, D. le Bolloc'h, P. Foury-Leylekian, J.-P. Pouget, R. Currat, P. Monceau, M. Krisch, Phys. Rev. B 69 (2004) 115113.
[64] G. Travaglini, I. Mörke, P. Wachter, Solid State Commun. 45 (1983) 289.
[65] J. Demsar, K. Biljaković, D. Mihailovic, Phys. Rev. Lett. 83 (1999) 800.
[66] D. Feinberg, J. Friedel, J. Phys. 49 (1988) 485.
[67] D. Feinberg, J. Friedel, Imperfections of charge density waves in blue bronzes, in: C. Schlenker (Ed.), Low-Dimensional Electronic Properties of Molybdenum Bronzes and Oxides, Kluwer Acad. Publ., Dordrecht, 1989, pp. 407–448.
[68] B. Hennion, J.-P. Pouget, M. Sato, Phys. Rev. Lett. 68 (1992) 2374;
J.-P. Pouget, B. Hennion, M. Sato, Phys. Rev. Lett. 69 (1992) 3266.
[69] E. Agoritsas, V. Lecomte, T. Giamarchi, Physica B 407 (2012) 1725.
[70] D. DiCarlo, E. Sweetland, M. Sutton, J.D. Brock, R.E. Thorne, Phys. Rev. Lett. 70 (1993) 845.
[71] H. Requardt, F.Ya. Nad, P. Monceau, R. Currat, J.E. Lorenzo, S. Brazovskii, N. Kirova, G. Grübel, Ch. Vettier, Phys. Rev. Lett. 80 (1998) 5631.
[72] V.L.R. Jacques, D. Le Bolloc'h, S. Ravy, J. Dumas, C.V. Colin, C. Mazzoli, Phys. Rev. B 85 (2012) 035113.
[73] T. Tamegai, K. Tsutsumi, S. Kagoshima, Y. Kanai, M. Tani, H. Tmozawa, M. Sato, K. Tsuji, J. Harada, M. Sakata, T. Nakajima, Solid State Commun. 51 (1984) 585.
[74] Y. Li, L.G. Lemay, J.H. Price, K. Cicak, K. O'Neill, K. Ringland, K.D. Finkelstein, J.D. Broch, R.E. Thorne, Phys. Rev. Lett. 83 (1999) 3514.
[75] E. Pinsolle, N. Kirova, V.L.R. Jacques, A.A. Sinchenko, D. Le Bolloc'h, Phys. Rev. Lett. 109 (2012) 256402.
[76] D. Le Bolloc'h, S. Ravy, J. Dumas, J. Marcus, F. Livet, C. Detlefs, F. Yakhou, L. Paolasini, Phys. Rev. Lett. 95 (2005) 116401.
[77] V. Jacques, PhD thesis, Université Paris XI, 2009.
[78] Charge Density Waves in Solids, in: L.P. Gor'kov, G. Gruner (Eds.), Modern Problems in Condensed Matter Science, vol. 25, North Holland, Amsterdam, 1989.
[79] S. Brazovskii, T. Nattermann, Adv. Phys. 53 (2004) 177.
[80] S. Ravy, J.-P. Pouget, R. Comès, J. Phys. I 2 (1992) 1173.
[81] S. Ravy, J.-P. Pouget, J. Phys. IV 3 (1993) 109.
[82] S. Ravy, J. Phys. IV 12 (2002) Pr6–Pr7.
[83] A. Rosso, T. Giamarchi, Phys. Rev. B 68 (2003) 140201(R);
A. Rosso, T. Giamarchi, Phys. Rev. B 70 (2004) 224204.
[84] L. Forro, L. Zuppiroli, J.-P. Pouget, K. Bechgaard, Phys. Rev. B 27 (1983) 7600.
[85] S. Brazovskii, J.-P. Pouget, S. Ravy, S. Rouzière, Phys. Rev. B 55 (1997) 3426.
[86] S. Ravy, S. Rouzière, J.-P. Pouget, S. Brazovskii, J. Marcus, J.-F. Bérar, E. Elkaim, Phys. Rev. B 74 (2006) 174102.
[87] I. Tüttő, A. Zawadowski, Phys. Rev. B 32 (1985) 2449.
[88] S. Rouzière, S. Ravy, J.-P. Pouget, S. Brazovskii, Phys. Rev. B 62 (2000) R16231.
[89] J.-P. Pouget, S. Ravy, S. Rouzière, S. Brazovskii, J. Phys. IV 12 (2002) Pr9-9.
[90] (a) This corrects the error of sign of Z in the argument developed in Ref. [88];
(b) In that case I_a' should be given by expression (5) of Ref. [88] with the phase shift bring by each soliton $\eta = \pi/2$ being opposite to the phase shift of the FOs.
[91] J.-P. Pouget, Physica B 460 (2015) 45.
[92] (a) D.J. Scalapino, J.E. Hirsch, J. Phys. (Paris) 44 (1983) C3-1507;
(b) J.E. Hirsch, D.J. Scalapino, Phys. Rev. B 27 (1983) 7169;
(c) J.E. Hirsch, D.J. Scalapino, Phys. Rev. B 29 (1984) 5554.
[93] N. Kirova, S. Brazovskii, Physica B 404 (2009) 382.
[94] J. van den Brink, D.I. Khomskii, J. Phys. Condens. Matter 20 (2008) 434217.
[95] G. Giovannetti, S. Kumar, J.-P. Pouget, M. Capone, Phys. Rev. B, Condens. Matter 85 (2012) 205146.
[96] M.H. Whangbo, E. Canadell, P. Foury, J.-P. Pouget, Science 252 (1991) 96.
[97] P. Foury, J.-P. Pouget, Int. J. Mod. Phys. B 7 (1993) 3973.
[98] J.P. Gaspard, R. Ceolin, Solid State Commun. 84 (1992) 839.
[99] D.-K. Seo, R. Hoffmann, J. Solid State Chem. 147 (1999) 26.
[100] K. Rossnagel, J. Phys. Condens. Matter 23 (2011) 213001.
[101] J.-C. Marmeggi, P. Haen, A. Filhol, P. Bastie, J. Phys. Conf. Ser. 592 (2015) 012035.
[102] L. Fast, O. Eriksson, B. Johansson, J.M. Wills, G. Straub, H. Roeder, L. Nordström, Phys. Rev. Lett. 81 (1998) 2978.
[103] G. Campi, D. Innocenti, A. Bianconi, J. Supercond. Nov. Magn. 28 (2015) 1355.
[104] J.M. Tranquada, Physica B 460 (2015) 136.
[105] B.I. Halperin, T.M. Rice, Solid State Phys. 21 (1968) 115.
[106] D. Jérome, J. Supercond. Nov. Magn. 25 (2012) 633.
[107] A. Ardavan, S. Brown, S. Kagoshima, K. Kanoda, K. Kuroki, H. Mori, M. Ogata, S. Uji, J. Wosnitza, J. Phys. Soc. Jpn. 81 (2012) 011004.
[108] C. Gros, R. Werner, Phys. Rev. B 58 (1998) R14677.
[109] E. Tutiš, S. Barišić, Phys. Rev. B 43 (1991) 8431.
[110] J.-P. Pouget, B. Hennion, M. Sato, J. Phys. IV 3 (1993) 215.